STATE OF THE CLIMATE IN 2022

ANTARCTICA AND THE SOUTHERN OCEAN

Kyle R. Clem and Marilyn N. Raphael, Eds.

Special Online Supplement to the *Bulletin of the American Meteorological Society* Vol. 104, No. 9, September, 2023

https://doi.org/10.1175/BAMS-D-23-0077.1

Corresponding author: Kyle R. Clem / kyle.clem@vuw.ac.nz

STATE OF THE CLIMATE IN 2022
Antarctica and the Southern Ocean

Editors

Ellen Bartow-Gillies
Jessica Blunden
Tim Boyer

Chapter Editors

Peter Bissolli
Kyle R. Clem
Howard J. Diamond
Matthew L. Druckenmiller
Robert J. H. Dunn
Catherine Ganter
Nadine Gobron
Gregory C. Johnson
Rick Lumpkin
Ademe Mekonnen
John B. Miller
Twila A. Moon
Marilyn N. Raphael
Ahira Sánchez-Lugo
Carl J. Schreck III
Richard L. Thoman
Kate M. Willett
Zhiwei Zhu

Technical Editor

Lukas Noguchi

BAMS Special Editor for Climate

Michael A. Alexander

American Meteorological Society

Cover Credit:
Photograph taken near the Dry Valleys, Antarctica in January 2022 by David Mikolajczyk, Antarctic Meteorological Research and Data Center, SSEC, UW-Madison, Madison, WI.

How to cite this document:
Antarctica and the Southern Ocean is one chapter from the *State of the Climate in 2022* annual report and is available from https://doi.org/10.1175/BAMS-D-23-0077.1. Compiled by NOAA's National Centers for Environmental Information, *State of the Climate in 2022* is based on contributions from scientists from around the world. It provides a detailed update on global climate indicators, notable weather events, and other data collected by environmental monitoring stations and instruments located on land, water, ice, and in space. The full report is available from https://doi.org/10.1175/2023BAMSStateoftheClimate.1.

Citing the complete report:
Blunden, J., T. Boyer, and E. Bartow-Gillies, Eds., 2023: "State of the Climate in 2022". Bull. Amer. Meteor. Soc., 104 (9), Si–S501 https://doi.org/10.1175/2023BAMSStateoftheClimate.1.

Citing this chapter:
Clem, K. R. and M. N. Raphael, Eds., 2023: Antarctica and the Southern Ocean [in "State of the Climate in 2022"]. Bull. Amer. Meteor. Soc., 104 (9), S322–S365, https://doi.org/10.1175/BAMS-D-23-0077.1.

Citing a section (example):
MacFerrin, M., T. Mote, A. Banwell, and T. Scambos, 2023: Ice-sheet seasonal melt extent and duration [in "State of the Climate in 2022"]. Bull. Amer. Meteor. Soc., 104 (9), S339–S341, https://doi.org/10.1175/BAMS-D-23-0077.1.

Editor and Author Affiliations (alphabetical by name)

Adusumilli, Susheel, Scripps Institution of Oceanography, University of California, San Diego, La Jolla, California

Baiman, Rebecca, Department of Atmospheric and Oceanic Sciences, University of Colorado Boulder, Boulder, Colorado

Banwell, Alison F., Earth Science Observation Center, Cooperative Institute for Research in Environmental Sciences (ESOC/CIRES), University of Colorado Boulder, Boulder, Colorado

Barreira, Sandra, Argentine Naval Hydrographic Service, Buenos Aires, Argentina

Beadling, Rebecca L., Department of Earth and Environmental Science, Temple University, Philadelphia, Pennsylvania

Bozkurt, Deniz, Department of Meteorology, University of Valparaíso, Valparaíso, Chile; Center for Climate and Resilience Research (CR)2, Santiago, Chile

Clem, Kyle R., School of Geography, Environment and Earth Sciences, Victoria University of Wellington, Wellington, New Zealand

Colwell, Steve, British Antarctic Survey, Cambridge, United Kingdom

Coy, Lawrence, Science Systems and Applications, Inc., Lanham, Maryland; NASA Goddard Space Flight Center, Greenbelt, Maryland

Datta, Rajashree T., Department of Atmospheric and Oceanic Sciences, University of Colorado Boulder, Boulder, Colorado

De Laat, Jos, Royal Netherlands Meteorological Institute (KNMI), DeBilt, The Netherlands

du Plessis, Marcel, Department of Marine Sciences, University of Gothenburg, Gothenburg, Sweden

Dunmire, Devon, Department of Atmospheric and Oceanic Sciences, University of Colorado Boulder, Boulder, Colorado

Fogt, Ryan L., Department of Geography, Ohio University, Athens, Ohio

Freeman, Natalie M., Department of Atmospheric and Oceanic Sciences, University of Colorado Boulder, Boulder, Colorado

Fricker, Helen A., Scripps Institution of Oceanography, University of California, San Diego, La Jolla, California

Gardner, Alex S., NASA Jet Propulsion Laboratory, Pasadena, California

Gille, Sarah T., Scripps Institution of Oceanography, University of California, San Diego, La Jolla, California

Johnson, Bryan, NOAA/OAR Earth System Research Laboratory, Global Monitoring Division, Boulder, Colorado; University of Colorado Boulder, Boulder, Colorado

Josey, Simon A., National Oceanography Centre, Southampton, United Kingdom.

Keller, Linda M., Antarctic Meteorological Research and Data Center, Space Science and Engineering Center, University of Wisconsin-Madison, Madison, Wisconsin

Kramarova, Natalya A., NASA Goddard Space Flight Center, Greenbelt, Maryland

Lazzara, Matthew A., Department of Physical Sciences, School of Arts and Sciences, Madison Area Technical College, Madison, Wisconsin; Antarctic Meteorological Research and Data Center, Space Science and Engineering Center, University of Wisconsin-Madison, Madison, Wisconsin

Lieser, Jan L., Australian Bureau of Meteorology and Institute for Marine and Antarctic Studies (IMAS), University of Tasmania, Hobart, Australia

MacFerrin, Michael, Earth Science and Observation Center, CIRES, University of Colorado, Boulder, Colorado

MacGilchrist, Graeme A., University of St. Andrews, St Andrews, United Kingdom; Princeton University, Princeton, New Jersey

MacLennan, Michelle L., Department of Atmospheric and Oceanic Sciences, University of Colorado Boulder, Boulder, Colorado

Massom, Robert A., Australian Antarctic Division, Australian Antarctic Program Partnership (AAPP) and Australian Centre for Excellence in Antarctic Science (ACEAS), Tasmania, Australia

Mazloff, Matthew R., Scripps Institution of Oceanography, University of California, San Diego, La Jolla, California

Mikolajczyk, David E., Antarctic Meteorological Research and Data Center, Space Science and Engineering Center, University of Wisconsin-Madison, Madison, Wisconsin

Mote, Thomas L., Department of Geography, University of Georgia, Athens, Georgia

Nash, Eric R., Science Systems and Applications, Inc., Lanham, Maryland; NASA Goddard Space Flight Center, Greenbelt, Maryland

Newman, Paul A., NASA Goddard Space Flight Center, Greenbelt, Maryland

Norton, Taylor, Antarctic Meteorological Research and Data Center, Space Science and Engineering Center, University of Wisconsin-Madison, Madison, Wisconsin

Ochwat, Naomi, Earth Science Observation Center, Cooperative Institute for Research in Environmental Sciences (ESOC/CIRES), University of Colorado Boulder, Boulder Colorado

Petropavlovskikh, Irina, NOAA/OAR Earth System Research Laboratory, Global Monitoring Division, Boulder, Colorado; University of Colorado Boulder, Boulder, Colorado

Pezzi, Luciano P., Laboratory of Ocean and Atmosphere Studies (LOA), Earth Observation and Geoinformatics Division (DIOTG), National Institute for Space Research (INPE), São José dos Campos, Brazil

Pitts, Michael, NASA Langley Research Center, Hampton, Virginia

Raphael, Marilyn N., Department of Geography, University of California, Los Angeles, Los Angeles, California

Reid, Phillip, Australian Bureau of Meteorology and Australian Antarctic Program Partnership (AAPP), Hobart, Australia

Santee, Michelle L., NASA Jet Propulsion Laboratory, Pasadena, California

Santini, Marcelo, Laboratory of Ocean and Atmosphere Studies (LOA), Earth Observation and Geoinformatics Division (DIOTG), National Institute for Space Research (INPE), São José dos Campos, Brazil

Scambos, Theodore, Earth Science Observation Center, Cooperative Institute for Research in Environmental Sciences (ESOC/CIRES), University of Colorado Boulder, Boulder, Colorado

Schultz, Cristina, Northeastern University, Boston, Massachusetts

Shi, Jia-Rui, Woods Hole Oceanographic Institution, Woods Hole, Massachusetts

Souza, Everaldo, Federal University of Pará (UFPA), Belém, Brazil

Stammerjohn, Sharon, Institute of Arctic and Alpine Research, University of Colorado Boulder, Boulder, Colorado

Strahan, Susan E., University of Maryland, Baltimore County, Baltimore, Maryland; NASA Goddard Space Flight Center, Greenbelt, Maryland

Thompson, Andrew F., California Institute of Technology, Pasadena, California

Trusel, Luke D., Pennsylvania State University, University Park, Pennsylvania

Wille, Jonathan D., Institute for Atmospheric and Climate Science, ETH Zürich, Zürich, Switzerland; Institut des Géosciences de l'Environnement, CNRS/UGA/IRD/G-INP, Saint Martin d'Hères, France

Yin, Ziqi, Department of Atmospheric and Oceanic Sciences, University of Colorado Boulder, Boulder, Colorado

Editorial and Production Team

Allen, Jessicca, Graphics Support, Cooperative Institute for Satellite Earth System Studies, North Carolina State University, Asheville, North Carolina

Camper, Amy V., Graphics Support, Innovative Consulting and Management Services, LLC, NOAA/NESDIS National Centers for Environmental Information, Asheville, North Carolina

Haley, Bridgette O., Graphics Support, NOAA/NESDIS National Centers for Environmental Information, Asheville, North Carolina

Hammer, Gregory, Content Team Lead, Communications and Outreach, NOAA/NESDIS National Centers for Environmental Information, Asheville, North Carolina

Love-Brotak, S. Elizabeth, Lead Graphics Production, NOAA/NESDIS National Centers for Environmental Information, Asheville, North Carolina

Ohlmann, Laura, Technical Editor, Innovative Consulting and Management Services, LLC, NOAA/NESDIS National Centers for Environmental Information, Asheville, North Carolina

Noguchi, Lukas, Technical Editor, Innovative Consulting and Management Services, LLC, NOAA/NESDIS National Centers for Environmental Information, Asheville, North Carolina

Riddle, Deborah B., Graphics Support, NOAA/NESDIS National Centers for Environmental Information, Asheville, North Carolina

Veasey, Sara W., Visual Communications Team Lead, Communications and Outreach, NOAA/NESDIS National Centers for Environmental Information, Asheville, North Carolina

6. Table of Contents

List of authors and affiliations S325
a. Overview S328
b. Atmospheric circulation and surface observations S329
Sidebar 6.1: The Antarctic heatwave of March 2022 ..... S333
c. Ice-sheet surface mass balance S336
d. Ice-sheet seasonal melt extent and duration S339
e. Ice-sheet mass balance S341
f. Sea-ice extent, concentration, and seasonality S344
Sidebar 6.2: Larsen B fast-ice breakout and initial glacier response S349
g. Southern Ocean S351
1. Sea-surface and mixed-layer properties S351
2. Upper-ocean heat content S354
3. Air–sea heat fluxes S354
4. Ocean biogeochemistry S355
h. 2022 Antarctic ozone hole S355
Acknowledgments S360
Appendix 1: Chapter 6 – Acronyms S361
References S362

Please refer to Chapter 8 (Relevant Datasets and Sources) for a list of all climate variables and datasets used in this chapter for analyses, along with their websites for more information and access to the data.

6. ANTARCTICA AND THE SOUTHERN OCEAN

Kyle R. Clem and Marilyn N. Raphael, Eds.

a. Overview

—K. R. Clem and M. N. Raphael

It was an extraordinary year in Antarctica and the surrounding Southern Ocean in 2022, marked by new records in temperature, surface mass balance, ice-sheet mass balance, surface melt, and sea ice. Many of these records can be linked to two strong and persistent atmospheric circulation anomalies: a deep Amundsen Sea Low that occupied the Bellingshausen, Amundsen, and Ross Seas for most of the year and a strong blocking high in the far southwest Pacific northeast of Wilkes Land, East Antarctica. These features directed warm, moist northerly flow to the Antarctic Peninsula/West Antarctica and East Antarctica, respectively, which was accompanied by an anomalously high number of landfalling atmospheric rivers (long and narrow regions of extreme poleward moisture transport), heavy snowfall, and well above-average surface mass balance in these two regions. This resulted in new record highs in net annual Antarctic surface mass balance and ice-sheet mass balance in 2022; this was the first time since 1993, the start of satellite-derived ice-sheet mass balance measurements, in which a positive net mass balance was observed in Antarctica, highlighting the extraordinary contribution of surface processes (i.e., snow accumulation) in 2022.

Offshore, these regions of persistent warm northerly flow, particularly across the Bellingshausen/Weddell Seas and the southeast Indian Ocean, enhanced sea-ice melt during the 2021/22 retreat season, prevented sea-ice growth during the autumn and winter advance phase, and led to early and rapid sea-ice retreat to start the 2022/23 retreat phase from late September onward; over 100 days of record-low sea-ice extent and sea-ice area were observed throughout 2022, including new all-time annual record lows in net sea-ice extent and area on the 25th and 21st of February 2022, respectively. Furthermore, on the eastern Peninsula, the warmth produced anomalously high surface melt across the Larsen Ice Shelf during the 2021/22 summer, punctuated by a record-breaking heatwave and surface melt event on the Peninsula in early February 2022. Combined with the large deficit of protective offshore sea ice in the Weddell Sea, which exposed the fast ice to open ocean swells, this contributed to the disintegration of a large area of decade-old fast ice in the remnant Larsen B embayment, as discussed in Sidebar 6.2. The breakup of fast ice was followed by rapid retreat and even collapse of upstream glaciers to which the fast ice had been attached. In East Antarctica, there was an unprecedented heatwave and coastal surface melt event in March due to a strong atmospheric river, which is detailed in Sidebar 6.1. Across a large portion of the high-elevation East Antarctic plateau, temperatures exceeded the previous March record maxima for several consecutive days, and a new all-time record-high temperature of –9.4°C (44°C above the March average) was set at Dome C II automated weather station on 18 March. Such high temperatures were especially remarkable to occur during March, which is the winter transition period characterized by rapid cooling on the plateau. Despite multiple historic warm events across Antarctica during the year, much of Antarctica closed the year with record to near-record-low temperatures and pressures associated with a strongly positive Southern Annular Mode pattern during November–December.

In the Southern Ocean, there were well-below-average annual-mean sea-surface temperatures (SSTs; 0.5 to 1.0°C below average) and above-average mixed layer depth in the South Pacific sector, which coincided with the enhanced storminess (more and/or deeper cyclones)

across the Amundsen Sea Low region through most of the year. In the South Atlantic, SSTs were well above average through the year, especially from September to December, likely due in part to the expansive open water across the northern Weddell Sea that is normally occupied by reflective sea ice. Finally, the Antarctic ozone hole re-emerged in early September and was the 18th largest (near average) in the 43-year satellite observational record. Following a similar seasonal development seen in 2020 and 2021, the 2022 ozone hole had a slower-than-average growth rate that is consistent with ozone recovery; however, also like the previous two years, the ozone hole was very long-lived due to weaker-than-average planetary wave activity from September through early November, and it did not break up until 16 December.

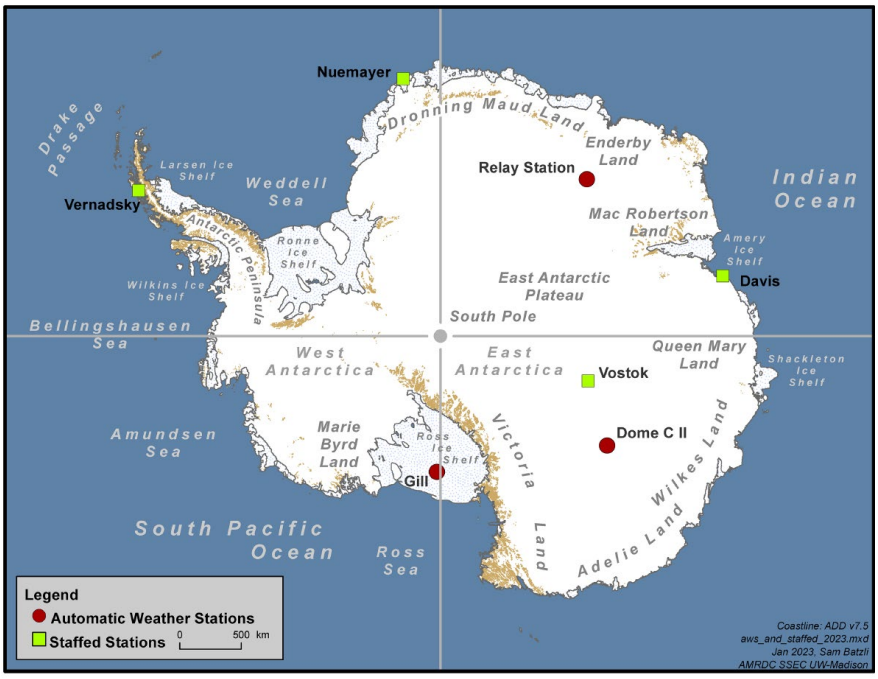

Fig. 6.1. Map of stations and geographic regions discussed in this chapter.

More details on Antarctica's climate and cryosphere, the Southern Ocean, and the ozone hole for 2022 are presented in this chapter. In most cases, where data are available, 2022 anomalies and standard deviations are based on the 1991–2020 climatological average. Otherwise, the climatological period is provided within each section. The geographical locations of place names mentioned throughout the chapter are provided in Fig. 6.1.

b. Atmospheric circulation and surface observations

—K. R. Clem, S. Barreira, S. Colwell, R. L. Fogt, L. M. Keller, M. A. Lazzara, D. E. Mikolajczyk, and T. Norton

Many of the major climate themes over Antarctica and the surrounding Southern Ocean in 2022 were a continuation of those seen during 2021. Most notable was the persistence of a deep Amundsen Sea Low (Clem et al. 2022) over the South Pacific, which produced another warm year on the Antarctic Peninsula; it was the second-warmest year on record for all five of the long-term staffed weather stations located on the Peninsula. Coupled with above-normal pressure over much of the southern middle latitudes and generally weak- to below-average pressure elsewhere over Antarctica, the Southern Annular Mode (SAM; Marshall 2003), the difference in pressure anomalies between the southern middle latitudes and Antarctica, remained in a strongly positive state through most of the year (except June), and 2022 saw the third-highest annual-mean SAM index on record (since 1957). This reflects a remarkably persistent positive SAM pattern over the Southern Hemisphere that dates back to October 2020: 24 of the past 27 months have recorded a positive monthly-mean SAM index. Furthermore, the persistence of La Niña through all of 2022 (see section 4b for details), combined with positive SAM conditions, enhanced the deepening and expansion of the Amundsen Sea Low (Fogt et al. 2011), especially from July onward when La Niña strengthened. This contributed to three of the five Peninsula stations recording their warmest July–December period on record. Lastly, there were two exceptional warming events in 2022 due to strong atmospheric rivers: one in early February on the Antarctic Peninsula (not shown; Gorodetskaya et al. 2023) and one in March on the East Antarctic plateau (see Sidebar 6.1 for details). A detailed overview of other noteworthy climate and circulation anomalies across Antarctica in 2022 is provided below.

Atmospheric circulation anomalies were examined using the European Centre for Medium-Range Weather Forecasts Reanalysis version 5 (ERA5; Hersbach et al. 2020). Figure 6.2 shows the monthly geopotential height (Fig. 6.2a) and temperature (Fig. 6.2b) anomalies averaged over the polar cap (60°S–90°S) and the monthly circumpolar zonal wind anomalies (Fig. 6.2c) averaged over 50°S–70°S. Surface climate anomalies were grouped into three periods of relatively persistent features: January–March, April–October, and November–December (Fig. 6.3). Monthly temperature and pressure anomalies are also shown for select Antarctic staffed and automated weather stations (AWS; Fig. 6.4; see Fig. 6.1 for station locations).

Pressure/geopotential height over the southern polar cap was near the long-term average for most of 2022 (Fig. 6.2a) before decreasing significantly in November–December. The only noteworthy exceptions were lingering negative geopotential height anomalies in the stratosphere (above 200 hPa) in January, tied to one of the longest-lived ozone holes on record in 2021 (Kramarova et al. 2022), and the redevelopment of negative geopotential height anomalies and the ozone hole in the stratosphere around September 2022 (see section 6h for discussion of the 2022 Antarctic ozone hole). These anomalies propagated downward into the lower troposphere during November and December, likely contributing to the strong negative surface pressure anomalies (–8 to –10 hPa) over the continent in these months. Stratospheric temperature anomalies generally followed the geopotential height anomalies (Fig. 6.2b), with strong negative temperature anomalies in January 2022 that redeveloped in August and thereafter peaked in October and November at around 6°C–8°C (0.5–1 std. dev.) below the 1991–2020 average; there was also a modest stratospheric cooling event from April to June that peaked in May (1.5°C [1.5 std. dev.] below average). In the troposphere, temperatures averaged over the polar cap were generally about 1°C warmer (1–1.5 std. dev.) than average from February onward. The most noteworthy polar cap-wide warming event occurred in June, coinciding with positive surface pressure anomalies observed everywhere across the continent except on the Peninsula (Fig. 6.4) and the only month in which the SAM index was negative during 2022 (Fig. 6.2). There were no months with below-average tropospheric temperatures when averaged over the polar cap; however, there were several significant regional cold events throughout the year (Fig. 6.4).

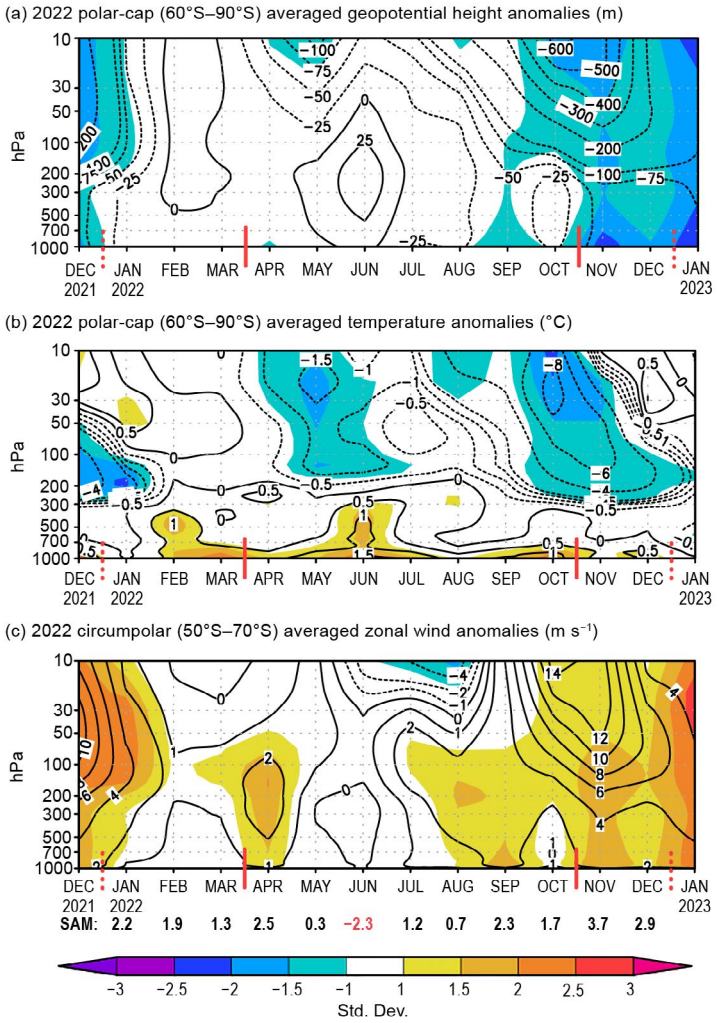

Fig. 6.2. Area-averaged (weighted by cosine of latitude) monthly anomalies over the southern polar region in 2022 relative to 1991–2020: (a) polar cap (60°S–90°S) averaged geopotential height anomalies (m; contour interval is 25 m up to ±100 m and 100 m after ±100 m); (b) polar cap averaged temperature anomalies (°C; contour interval is 0.5°C up to ±2°C and 2°C after ±2°C); (c) circumpolar (50°S–70°S) averaged zonal wind anomalies (m s^{-1}; contour interval is 2 m s^{-1} with an additional contour at ±1 m s^{-1}). Shading depicts standard deviation of monthly anomalies as indicated by color bar at bottom. Red vertical bars indicate the three climate periods used for compositing in Fig. 6.3; the dashed lines near Dec 2021 and Dec 2022 indicate circulation anomalies wrapping around the calendar year. Values from the Marshall (2003) Southern Annular Mode (SAM) index are shown below (c) in black (positive values) and red (negative values). (Source: ERA5.)

Consistent with the positive SAM pattern, circumpolar westerly winds were near or above their long-term average strength throughout the troposphere and stratosphere during the year (Fig. 6.2c). A few significant intensifications of the tropospheric westerlies in April, August–September, and November–December coincided with the highest monthly SAM index values of the year. Meanwhile, the strength of the stratospheric westerlies followed the same pattern as the stratospheric pressure and temperature anomalies, including a continued stronger-than-average polar vortex in January and the redevelopment of a stronger-than-average polar vortex in September, with westerly wind speeds 10 m s^{-1} to 15 m s^{-1} (1–1.5 std. dev.) above the long-term mean in November.

The surface pressure and temperature anomalies in Fig. 6.3 illustrate the impressive persistence and extent of the deep Amundsen Sea Low and associated warm conditions across the Peninsula region during the year. From January to March, below-average surface pressures of more than −6 hPa (2 std. dev.) were located in the Amundsen and Ross Seas extending onto adjacent areas of West Antarctica and the Ross Ice Shelf (Fig. 6.3a) along with above-normal temperatures in the Amundsen Sea Embayment and northeast Peninsula (Fig. 6.3b). South of New Zealand and Tasmania, an exceptionally strong positive pressure anomaly of >6 hPa (3 std. dev.) was present, coupled with below-average pressure off the coast of East Antarctica near 90°E. These features reflect the circulation pattern that produced the exceptional warming event on the East Antarctic plateau in March (see Sidebar 6.1), where Dome C II AWS (Fig. 6.4e) recorded its second-warmest March on record (5.4°C above the March average), and contributed to positive temperature anomalies of +1 to +2°C (1–2 std. dev.) on the plateau and Ross Ice Shelf. Lastly, a short-lived but strong zonal wave 3 pattern (three positive-negative pressure anomaly pairs over the Southern Ocean; Raphael 2007) occurred in January (not shown), which produced warm northerly flow onto Dronning Maud Land where Relay Station AWS recorded its warmest January on record at –25.8°C (3.1°C above average).

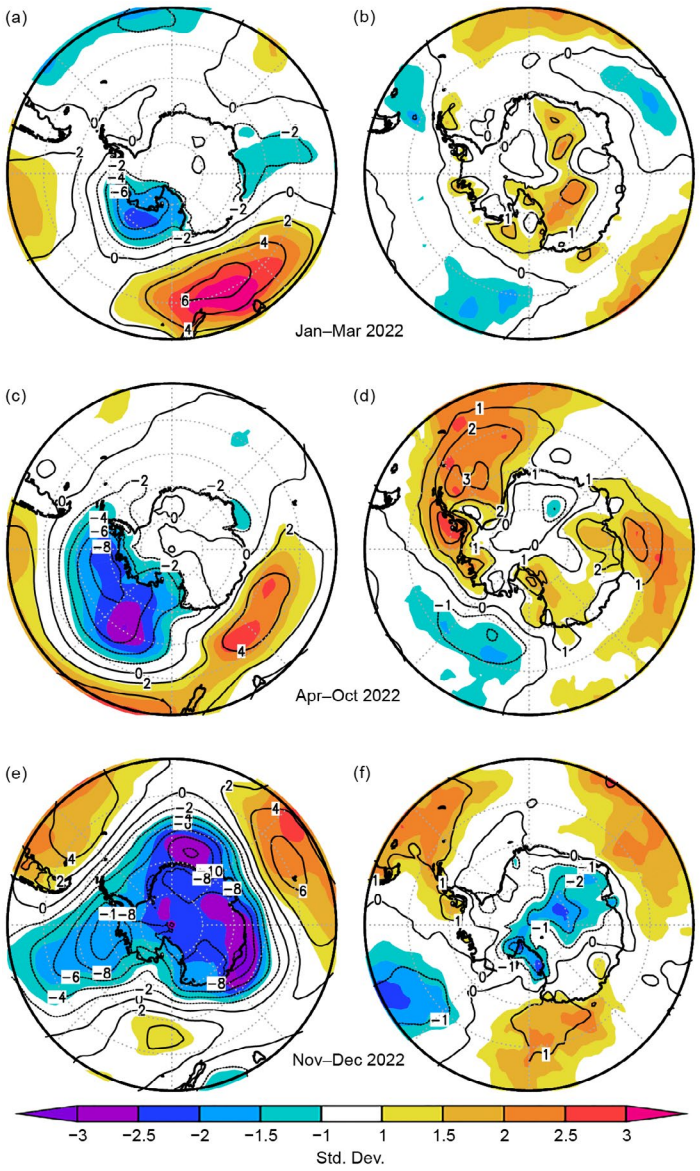

Fig. 6.3. (left) Surface pressure (hPa) and (right) 2-m temperature anomalies (°C) relative to 1991–2020 for (a),(b) Jan–Mar 2022; (c),(d) Apr–Oct 2022; and (e),(f) Nov–Dec 2022. Contour interval is 2 hPa for surface pressure anomalies and 1°C for 2-m temperature anomalies. Shading shows the standard deviation of the anomalies. (Source: ERA5.)

From April onward, the Amundsen Sea Low deepened and gradually grew in size (Fig. 6.3c), albeit with a sudden and short-lived eastward shift from the Ross Sea to the Bellingshausen Sea in June (not shown), illustrated by the rapid reversal of pressure anomalies between Gill AWS on the Ross Ice Shelf (Fig. 6.4f) and Vernadsky on the western Peninsula (Fig. 6.4a). Throughout April–October, seven-month average temperature anomalies of +1°C to +3°C (1.5–2.5 std. dev.) encompassed a vast region of the southeast Pacific and South Atlantic, including the Antarctic Peninsula. The evolution and significance of these positive temperature anomalies were captured

at Vernadsky, including two new record-high monthly temperatures recorded in August (4.8°C above average) and September (4.7°C above average). Other notable temperature records on the Antarctic Peninsula (not shown) include the warmest spring for Vernadsky and Bellingshausen, the warmest August at Rothera, and the warmest November at Bellingshausen.

Elsewhere around Antarctica, surface pressure and temperature anomalies were highly variable from April to October. Dome C II AWS experienced a dramatic flip from its second-warmest March on record to its coldest April on record (4.1°C below average) as cold offshore flow developed in this region on the southwest side of the Amundsen Sea Low. Neumayer (Fig. 6.4b) experienced anomalously warm conditions from April to June followed by an anomalously cold August. Farther east at Davis (Fig. 6.4c), anomalously warm conditions developed from June to October (Fig. 6.3d) with the development of a deep cyclone west of Davis that produced warm northerly flow to this region.

In the final two months of the year, strong negative surface pressure anomalies of –8 hPa to –10 hPa (2–3 std. dev.) developed over much of the continent, and the circumpolar pattern transitioned to a prominent zonal wave 3 structure (Fig. 6.3e). This produced three distinct regions of warm northerly flow in the South Atlantic, Indian, and southwest Pacific Oceans, while below-average temperature anomalies of –1°C to –2°C (0.5–1.5 std. dev.) developed over the interior (Fig. 6.3f). All six stations experienced well-below-average pressure anomalies ranging from –5 hPa to –12 hPa during November and December. Numerous new record-low monthly pressures were recorded: Neumayer, Relay Station AWS, and Dome C II AWS all recorded their lowest November pressure on record, while Davis recorded its lowest pressure on record for both November and December. Some of the coldest temperatures occurred on the Ross Ice Shelf, where Gill AWS recorded its coldest November on record.

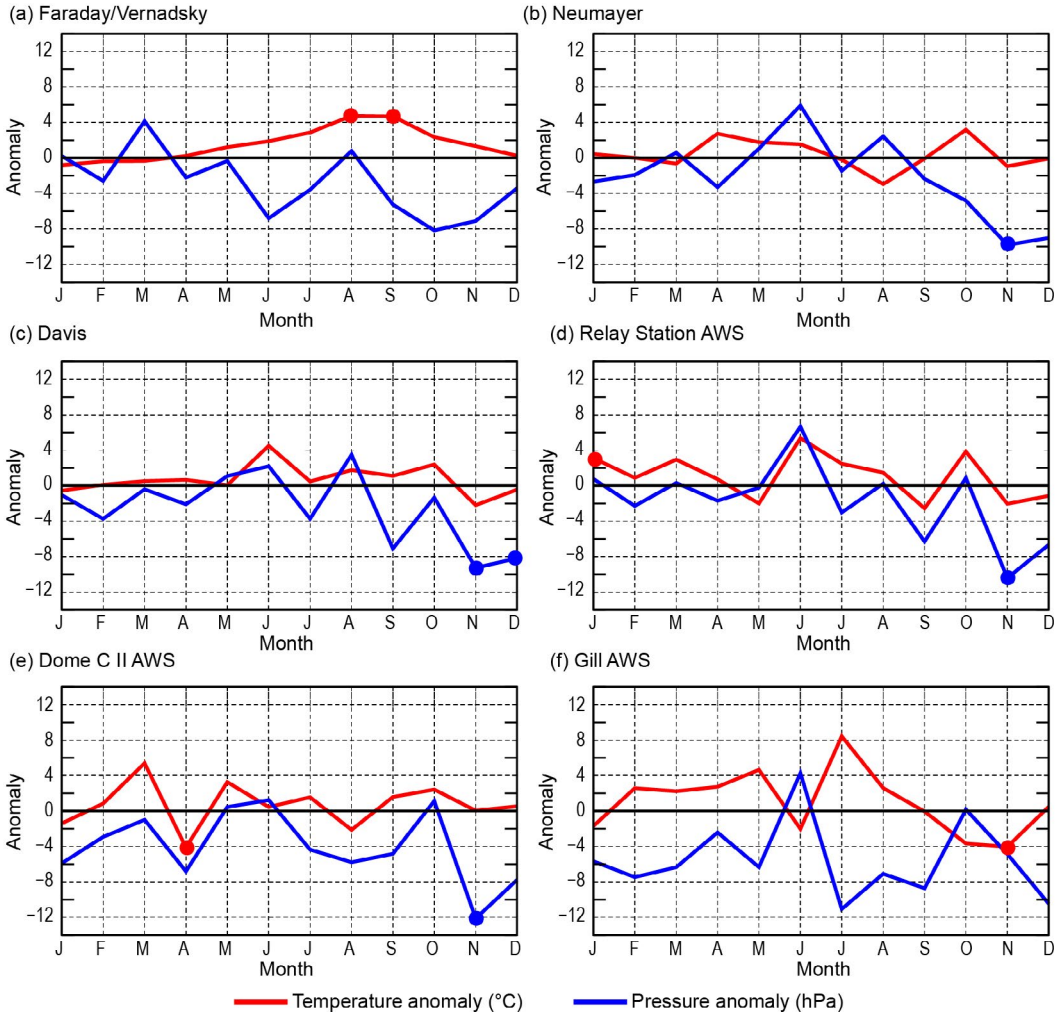

Fig. 6.4. Observed monthly Antarctic climate anomalies during 2022 from six representative stations (three staffed [a]–[c] and three automatic [d]–[f]). Anomalies for temperature (°C) are shown in red and mean sea-level pressure/surface pressure (hPa) are shown in blue, with filled circles denoting monthly-mean records set for each station in 2022. All anomalies are based on the monthly 1991–2020 averages where possible. The station observation records start in 1950 for Vernadsky, 1981 for Neumayer, 1957 for Davis, 1995 for Relay Station automated weather station (AWS), 1980 for Dome C II AWS, and 1985 for Gill AWS. See Fig. 6.1 for station locations.

Sidebar 6.1: The Antarctic heatwave of March 2022

—R. T. DATTA, J. D. WILLE, D. BOZKURT, D. E. MIKOLAJCZYK, K. R. CLEM, Z. YIN, AND M. MACFERRIN

In the middle of March 2022, East Antarctica experienced an unprecedented, large-scale heatwave, despite March historically marking the transition to Antarctic winter. This event was associated with an intense atmospheric river, which reached deep into the Antarctic interior, and was shortly followed by the collapse of the critically-unstable Conger Ice Shelf. While short-lived and unprecedented, these intense phenomena are more probable in future climate scenarios, with impacts including both enhanced precipitation and surface melt (Wille et al. 2023).

Temperatures

Between 14 and 20 March, temperatures over a large region of East Antarctica exceeded 10°C above the March climatological mean (Fig. SB6.1a), both at the coast and inland over the cold interior. The Dome C II automatic weather station (AWS) located high on the plateau at 3250 m a.s.l. (shown in green), captured the evolution of the heatwave at a high temporal resolution. For the first half of March, temperatures were near the Dome C II AWS March climatological mean of –53.4°C and ranged from around –45°C to –60°C (Fig. SB6.1b).

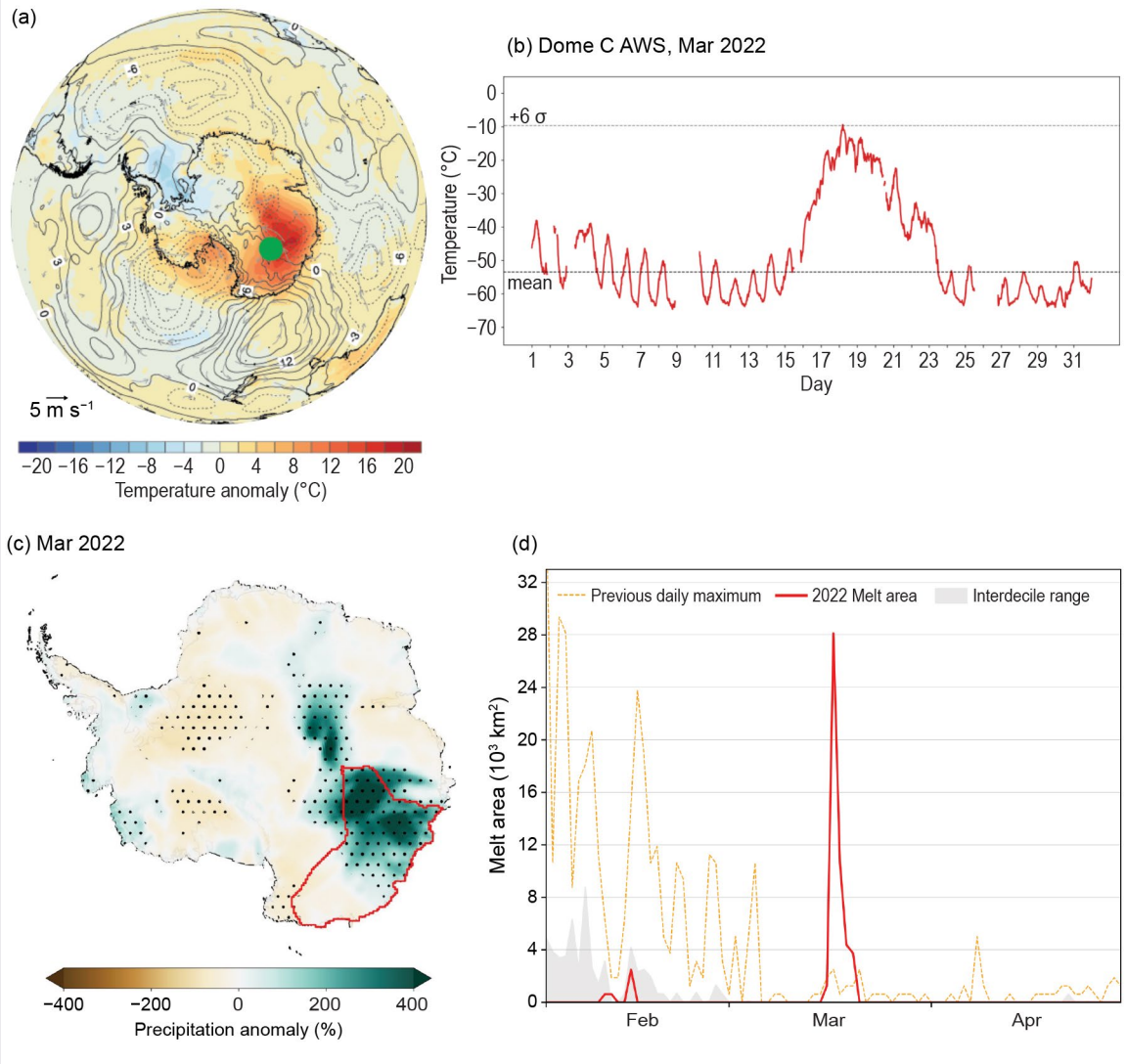

Fig. SB6.1. (a) Mean 2-m temperature anomaly (°C) for 14–20 Mar 2022 as compared to the 1991–2020 Mar mean (Source: ERA5) and (b) UW-Madison Dome C II automated weather station (AWS; 75.106°S, 123.347°E) 10-min quality-controlled temperature observations for Mar 2022 (°C; red line). The black horizontal dashed line denotes the Dome C II March climatological mean temperature (–53.4°C). The gray dashed line denotes the temperature (–9.6°C) 6 std. dev. above the mean, where 1 std. dev. is ±7.3°C. (c) ERA5-Total precipitation anomaly (%) for Mar 2022 as compared to the 1991–2020 reference period with Wilkes and Adélie Land region outlined in red. (d) Surface melt area (× 10³ km²) over the Wilkes and Adélie Land region outlined in (d) as retrieved from passive microwave.

Temperatures followed a general cooling pattern with the onset of winter and exhibited diurnal cycles typical of March at this site. Beginning midday on 15 March, temperatures began a rapid and steady increase that overwhelmed the diurnal cycle signature, as the pressure and wind speeds also increased (not shown). The temperature reached a maximum of –9.4°C on 18 March at 04:40 UTC, establishing a new all-time high temperature record at the Dome C II AWS and breaking the previous all-time high temperature of –10.0°C set in the peak of summer on 2 January 2002. The occurrence of this record during the transition to winter is especially remarkable as the high-elevation interior ice sheet is marked by extreme radiational cooling during this time. Thereafter, temperatures only gradually decreased and did not return to normal until 23 March. For the remainder of the month, temperatures resumed the typical diurnal cycle pattern about the climatological average of around –60°C.

Impacts

The impacts on the surface of the ice sheet included an increase in both rain and snowfall as well as a short period of intense surface melt. Within the larger Wilkes and Adélie region, total precipitation in March from European Centre for Medium-Range Weather Forecasts Reanalysis version 5 (ERA5) exceeded 300% of the 1991–2020 climatological mean for the month of March (Fig. SB6.1c), contributing to 2022 having the highest annual surface mass balance in at least four decades (see section 6c). Throughout East Antarctica, large increases in firn air content from snowfall gains were observed. Surface melt was limited to the coasts, geographically centered on the Holmes, Totten, and Moscow ice shelves. On 17 March, the region experienced a record-high maximum melt area of 28,100 km^2 (Fig. SB6.1d), more than doubling the previous record March melt area of 10,600 km^2 from 2002. It was the most extensive melt event recorded of any late-summer date beyond 4 February in the Wilkes and Adélie region of Antarctica since the beginning of the observational record in 1979. Additionally, the lack of sea ice and large swells associated with storms impacted the Conger ice shelf at the margins of this region (Wille et al. a,b submitted), which had been increasing in fragility in recent years and finally collapsed following this event (Baumhoer et al. 2021).

Large-scale drivers

The intruding burst of heat and moisture over East Antarctica was facilitated by the development of multiple moist tropical air masses over the Atlantic and Indian Oceans over several days that eventually merged and were directed toward the continent by a mid-level blocking ridge within a quasi-stationary zonal wave 3 pattern over the Southern Ocean (Fig. SB6.2). The evolution of this moisture can be seen in snapshots of integrated vapor transport from 10 March (Fig. SB6.2a in the Atlantic), strengthening over the Indian Ocean (Figs. SB6.2b,c) and finally reaching the continent on 16 March (Fig. SB6.2d). The intensified quasi-stationary mid-level ridge extending from New Zealand and southeast Australia toward

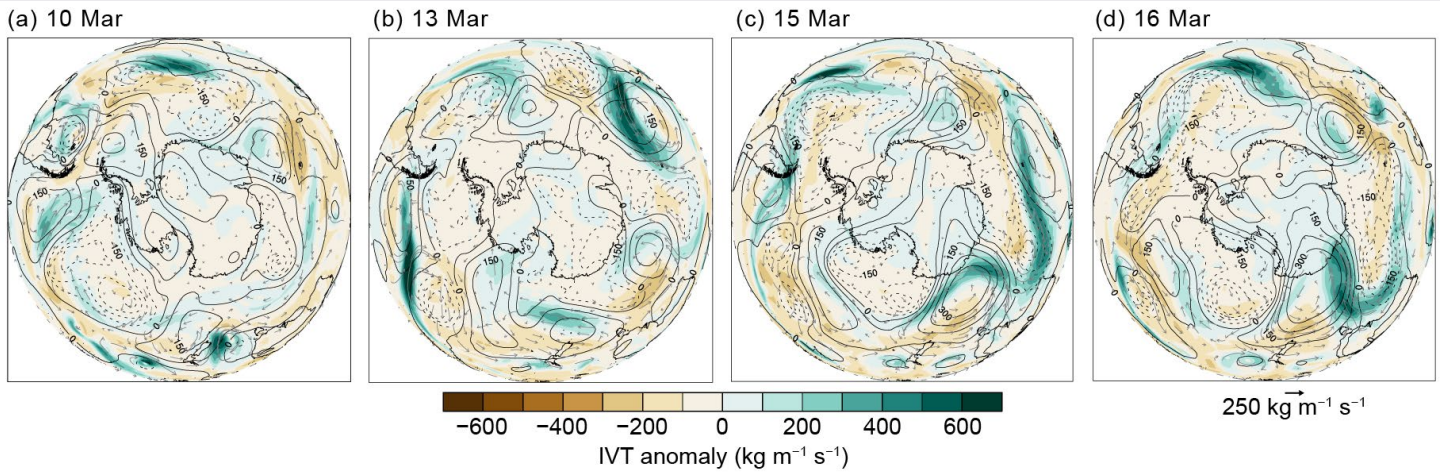

Fig. SB6.2. Snapshots of integrated water vapor transport (IVT) anomaly (kg m^{-1} s^{-1}) compared to the 1991–2020 reference period. Shown for (a) 10 Mar, (b) 13 Mar, (c) 15 Mar, and (d) 16 Mar. Vectors correspond to IVT vector deviations (zonal and meridional components) from the reference period. Also shown are 500-hPa geopotential height deviations (solid and dashed contours for positive and negative anomalies, respectively, every 75 m) from the 1991–2020 climatology. (Source: ERA5.)

East Antarctica and a mid-level trough on the western flank of the ridge during 15–16 March (Figs. SB6.2c,d) appeared crucial for the strong poleward meridional moisture transport within an intense atmospheric river (Fig. SB6.2d).

Atmospheric rivers are rare events that represent the transport of subtropical/midlatitude heat and moisture toward the polar regions. According to the polar-specific atmospheric river detection algorithm from Wille et al. (2021), a prolonged and intense atmospheric river was detected over East Antarctica during 14–18 March (Fig. SB6.3). The low-level moisture associated with the atmospheric river was transported by a warm conveyor belt into the upper troposphere leading to strong upper-level latent heat release from cloud formation. This ultimately led to strong diabatic modification of potential vorticity which further reinforced and entrenched the downstream atmospheric ridge creating blocking conditions (Wernli and Davies 1997).

The net impact of this intense atmospheric river primarily increased surface mass balance with enhanced snowfall. However, in future climate scenarios, higher temperatures may enhance the relative mass loss during atmospheric river events, as surface melt contributes to both runoff (reducing surface mass balance directly) and to the increased fragility of buttressing ice shelves.

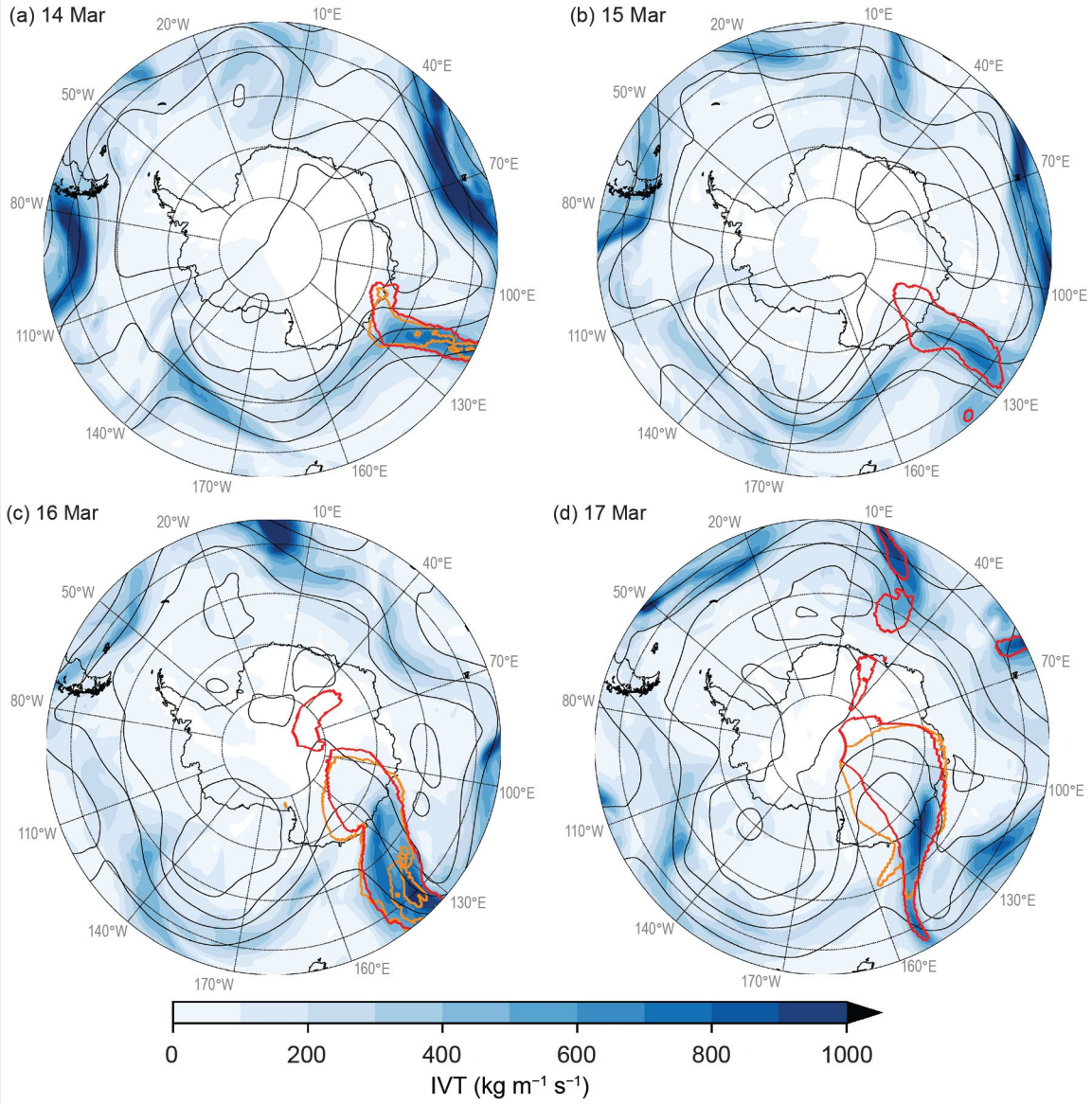

Fig. SB6.3. Atmospheric river shape. Integrated vapor transport (IVT; kg m^{-1} s^{-1}) in blue shading with the atmospheric river outline as detected by the meridional IVT (red outline) and integrated water vapor (IWV, orange outline) schemes in the detection algorithm described in Wille et al. (2021) along with 500-hPa geopotential height (contours). Shown for (a) 14 Mar, (b) 15 Mar, (c) 16 Mar, and (d) 17 Mar at 1200 UTC. (Source: MERRA2.)

c. Ice-sheet surface mass balance

—R. T. Datta, R. Baiman, Z. Yin, J. D. Wille, D. Dunmire, M. L. Maclennan, L. D. Trusel, and D. Bozkurt

Surface mass balance (SMB) represents the net effect of all processes that add or remove mass from the surface of an ice sheet. For the grounded Antarctic Ice Sheet (AIS), snowfall is the dominant SMB term, with approximately 2300 Gt accumulating each year (Agosta et al. 2019; Lenaerts and van den Broeke 2012; Mottram et al. 2021). Strong coast-to-plateau gradients in SMB exist across the AIS (Fig. 6.5b), with mass gains in coastal areas exceeding 500 mm water equivalent (w.e.) yr^{-1} compared to <50 mm w.e. yr^{-1} in the high-elevation interior of the East Antarctic Ice Sheet. At ice sheet wide and regional scales, as much as 40%–60% of annual snowfall results from "extreme precipitation events", defined as delivering snowfall in the top 10% of the long-term daily mean snowfall, often in the form of atmospheric rivers (ARs; Turner et al. 2019; Maclennan and Lenaerts 2021; Wille et al. 2021). These mass gains are countered by losses from sublimation, the leading negative SMB term for the AIS (Mottram et al. 2021). While surface melt and hydrology are extensive across AIS ice shelves (Bell et al. 2018; Bevan et al. 2020; Banwell et al. 2021; Arthur et al. 2022), and observations of lake drainages suggest some meltwater runoff exists (Dunmire et al. 2020; Trusel et al. 2022), nearly all AIS surface melt is thought to refreeze within the firn layer (the layer of partially compacted snow from previous years located beneath the new surface snow accumulation), making it a negligible term in the

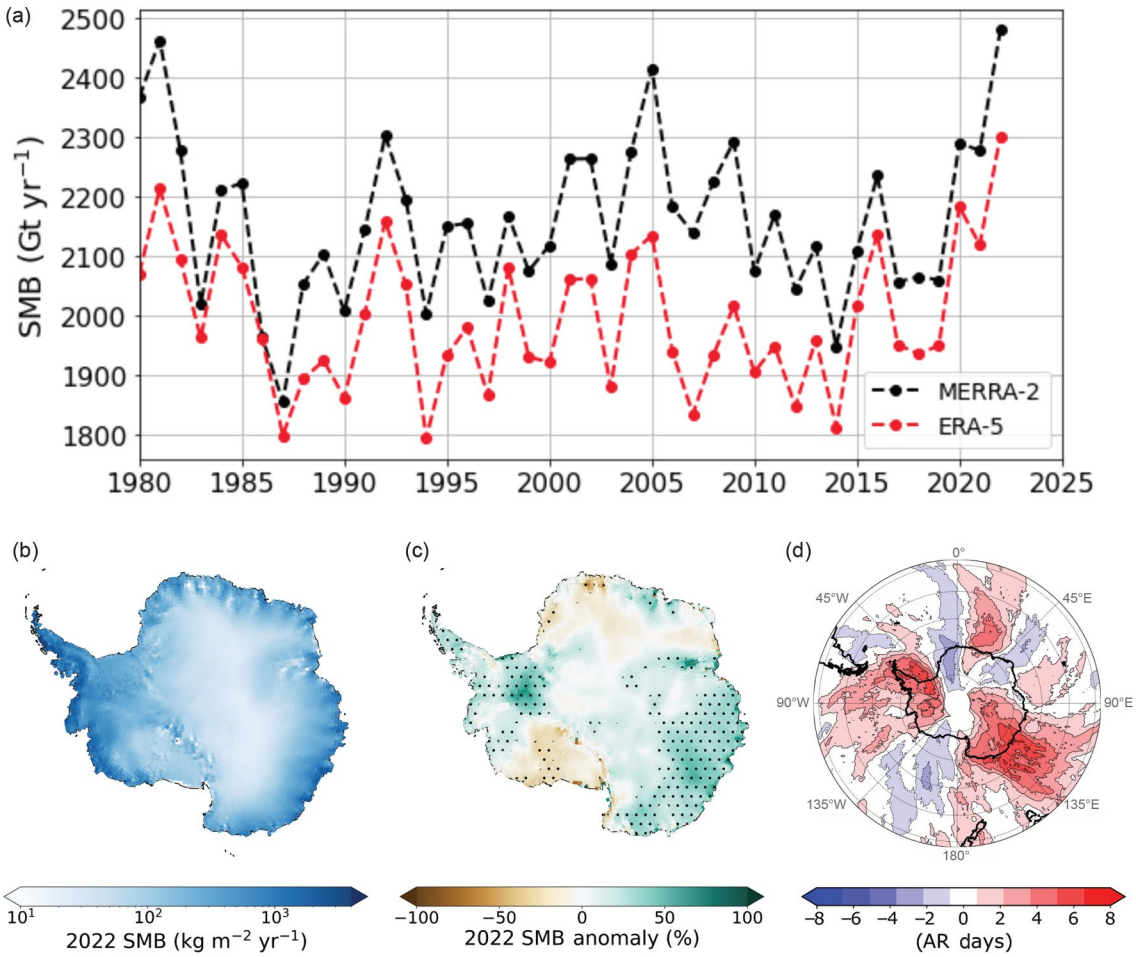

Fig. 6.5. (a) Time series of annual surface mass balance (SMB) in Gt (10^{12} kg) yr^{-1}. (b) MERRA-2 2022 SMB (kg m^{-2} yr^{-1}). (c) MERRA-2 2022 SMB anomaly relative to the 1991–2020 mean (%). The 2022 SMB anomaly is higher than the 1991–2020 standard deviation in the stippled areas. (d) 2022 atmospheric river occurrence anomaly (days) relative to the 1991–2020 mean from MERRA-2.

contemporary AIS SMB (van Wessem et al. 2018). It should be noted that despite its relatively small role in the total mass balance of the AIS, surface melt is an important indicator of processes and anomalies in the coastal regions with important consequences such as ice-shelf destabilization (discussed in section 6d). In future warming scenarios, surface melt is expected to intensify and play a more direct role in the AIS mass balance and ice shelf stability (Trusel et al. 2015; Kittel et al. 2021; Gilbert and Kittel 2021), while enhanced snowfall and SMB gains over the grounded ice sheet are also projected (Seroussi et al. 2020; Dunmire et al. 2022).

Global reanalysis products are useful tools to quantify AIS SMB in near-real time. Given negligible surface meltwater runoff in Antarctica today, AIS SMB can be reliably approximated as total precipitation minus surface evaporation and sublimation (i.e., P–E; e.g., Medley and Thomas 2019; Lenaerts et al. 2019; Mottram et al. 2021). Here, we use two reanalyses, Modern-Era Retrospective Analysis for Research and Applications version 2 (MERRA-2; at 0.5° × 0.625° horizontal resolution, Gelaro et al. 2017) and European Centre for Medium-Range Weather Forecasts Reanalysis version 5 (ERA5; at 0.25° horizontal resolution, Hersbach et al. 2020), to analyze the 2022 AIS SMB, its spatial and seasonal characteristics, and compare it to the 1991–2020 climatological period. Though important biases remain associated with, for example, ice sheet–cloud–radiation feedbacks and precipitation, evaluations of various reanalysis products over Antarctica indicate that MERRA-2 and ERA5 represent recent Antarctic climate and SMB well (Gossart et al. 2019; Medley and Thomas 2019; Wang et al. 2016).

In 2022, SMB (driven by snowfall) was the highest on record (since 1980), at 2480 Gt (MERRA-2) or 2302 Gt (ERA5), over the grounded ice sheet, as compared to the climatological mean of 2155±128 Gt yr^{-1} (MERRA-2) and 1977±105 Gt yr^{-1} (ERA5; Figs. 6.5a,b). Though the AIS SMB from ERA5 is significantly ($p<0.05$) drier than from MERRA-2 during the climatological period, both reanalyses have comparable interannual variations during the climatological period, and neither suggest a significant long-term trend in SMB (Fig. 6.5a). The 2022 AIS SMB was 2.5 std. dev. higher than the MERRA-2 climatological mean and 3.1 std. dev. higher than the ERA5 climatological mean. We note that the SMB estimates still need to be further validated to consider model uncertainties. Since both reanalysis datasets produce similar spatial results, we use MERRA-2 hereafter to focus on spatial characteristics of the 2022 SMB.

The historic high 2022 SMB is reflected spatially in Fig. 6.5c, indicating positive anomalies over much of West Antarctica with relative maxima around the northern Antarctic Peninsula and Palmer Land and Ellsworth Land in West Antarctica (>150% above the climatological mean), and over a broad swath (75°E–165°E) of East Antarctica including Victoria Land and Wilkes Land (>80% above the climatological mean). These regions of high SMB in 2022 coincide with regions of below-average sea ice in the surrounding ocean (section 6f) and anomalously high ice-sheet mass balance (section 6e). They also coincide with the deep and persistent Amundsen Sea Low (ASL) that was present for nearly all of 2022 and a strong blocking high pressure south of New Zealand and Tasmania from January through October (section 6b). The ASL produced warm northerly flow across the Peninsula and West Antarctic (section 6f), while the blocking high in the far southwest Pacific/southeast Indian Oceans, reflecting the pattern seen during the East Antarctic heatwave in March (see Sidebar 6.1), delivered warm northerly flow to large portions of East Antarctica for much of the year. Despite the magnitude of the 2022 SMB, portions of Dronning Maud Land and the Ross Sea region feature anomalously low SMB (<50% of the climatological mean). Regions with high SMB are coincident with regions experiencing anomalously high numbers of ARs (Fig. 6.5d), favored by the aforementioned blocking high/low pressure anomaly couplets shown in Fig. 6.3, triggering poleward heat and moisture transport.

The climatological AIS SMB varies considerably throughout the year (Fig. 6.6a), with a minimum in summer (124 Gt–172 Gt month^{-1}) and a maximum in austral fall and winter (195 Gt–220 Gt month^{-1}). In 2022, the SMB diverged substantially from the climatological mean in both MERRA-2 and ERA5 reanalyses in January (2.9 std. dev. above the mean in MERRA-2), March (2.5 std. dev.), July (2.9 std. dev.), September (1.6 std. dev.), and November (1.4 std. dev.; Fig. 6.6a). The positive SMB anomaly in January is attributed to high snowfall over Dronning Maud Laud in East Antarctica and the Amundsen Sea sector in West Antarctica. In March, the positive SMB

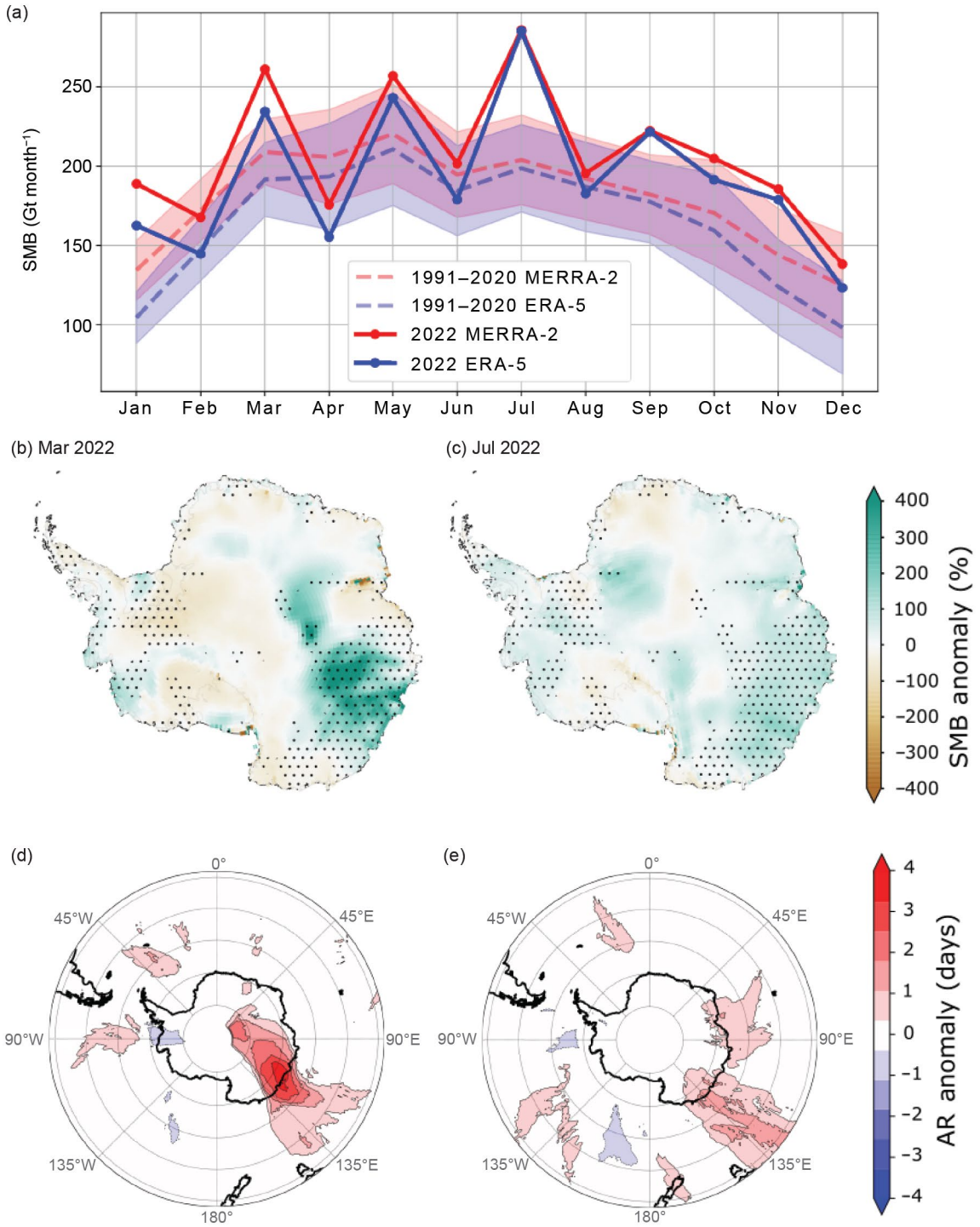

Fig. 6.6. (a) Seasonal cycle of (grounded) Antarctic Ice Sheet integrated surface mass balance (SMB) in Gt (10^{12} kg) month^{-1}, according to MERRA-2 (red) and ERA5 (blue), with 2022 value shown in solid line, 1991–2020 mean shown in a dashed line with shading showing 1 std. dev. MERRA-2 SMB anomaly for the month relative to the month's 1991–2020 mean for (b) Mar 2022 and (c) Jul 2022, with stippled areas indicating regions where the SMB anomaly is higher than the 1991–2020 1 std. dev. MERRA-2 anomaly (days) when an atmospheric river (AR) was detected for the month compared to the 1991–2020 mean for (d) Mar 2022 and (e) Jul 2022.

anomaly (up to 400%) was primarily driven by a powerful AR that made landfall in East Antarctica from 15 to 19 March, which is discussed in Sidebar 6.1. July saw near ice sheet-wide anomalously high SMB (contributing 12% of the total SMB in 2022), with the strongest anomalies across Wilkes Land driven by ARs as well as poleward heat and moisture advection enhanced by the atmospheric blocking south of Tasmania (Figs. 6.6c,e). This blocking is accompanied by positive SMB anomalies across Marie Byrd Land, the Antarctic Peninsula, and Ellsworth Land. Deep cyclones over the Ross Sea in September (Fig. 6.3c) and over the Antarctic Peninsula and most of East Antarctica in November (Fig. 6.3e) led to anomalously high SMB over the AIS in these months as well.

d. Ice-sheet seasonal melt extent and duration

—M. MacFerrin, T. Mote, A. Banwell, and T. Scambos

Surface melt on the Antarctic Ice Sheet (AIS) occurs primarily on the coastal margins, especially on the Antarctic Peninsula and on the ice shelves surrounding the continent. Surface melt runoff plays a relatively small role in the total mass balance of the AIS compared to far larger contributions from snow accumulation, iceberg calving, and basal melting of ice shelves and the ice sheet. However, surface melting can be seen as a vital measure of ice-sheet health as it has a large effect on increasing the density of underlying firn in areas of significant melting. If melt volume is a large fraction of the annual accumulation, surface melt can contribute to ice-shelf break up and upstream grounded glacier acceleration through hydrofracture (Scambos et al. 2014; Banwell et al. 2013). Since the austral melt season spans two calendar years, we focus here on melt season spanning October 2021 through April 2022. The 2022/23 Antarctic melt season will be discussed in next year's report.

Daily surface melt is mapped using satellite-derived passive-microwave brightness temperatures. The source data are distributed as daily composited polar stereographic brightness temperatures by the National Snow and Ice Data Center (Meier et al. 2019; Gloersen 2006) spanning 1979 through present day. Daily passive microwave brightness temperatures using the 37-GHz horizontal polarization as well as the 37- and 19-GHz 363 vertical polarization channels are acquired by the Scanning Multi-channel Microwave Radiometer (SMMR), Special Sensor Microwave Imager (SSM/I), and Special Sensor Microwave Imager/Sounder (SSMIS) sensors. The austral melt season is defined here as 1 October through 30 April. Although small, brief melt events can be measured along Antarctica's northern coastal margins during the austral winter, the vast majority of melt happens during these seven months, with the most typically in December and January. An ice-extent mask of 25-km grid cells for the AIS was developed from the Quantarctica v3.0 Detailed Basemap dataset (Norwegian Polar Institute 2018). The AIS is divided into seven melt extent and climate regions by clustering glaciological drainage basins (based on Shepherd et al. 2012; Fig. 6.8a). The methods used here were first developed to track Greenland's ice-sheet surface melting on a daily basis (Mote and Anderson 1995; Mote 2007, 2014), modified slightly to accommodate Antarctic surface conditions, as outlined in previous reports (MacFerrin et al. 2021, 2022).

According to the passive-microwave satellite observations, the 2021/22 melt season recorded slightly higher-than-average cumulative melt index (days × area) of 7.92 million km^2 days (Figs. 6.7a,c), about 5.1% greater than the median melt index of 7.54 million km^2 days during the 1990/91–2019/20 baseline period. However, this near-typical melt season averaged across the continent was punctuated by substantial spatial and temporal anomalies in individual regions. The Antarctic Peninsula (Fig. 6.8b) saw an annual melt index more than 31% above the baseline median value. Peninsula melt was affected by four consecutive extensive melt events in December and early January. Melting extended to an area of decade-old landfast ice in the embayment of the former Larsen B Ice Shelf, pre-conditioning it for a breakup that began on 18 January 2022

(see Sidebar 6.2). Late in the season on the Peninsula, a season-high melt event on 8 February covered a maximum area of 240,000 km^2 and broke the observational historical record for melt extent for the month of February, previously set at 233,000 km^2 on 1 February 1988. A majority of the area of the southern Larsen C and Larsen B-remnant ice shelves observed 30 more melt days than average (Fig. 6.7b). Indeed, Antarctica's cumulative melt index is dominated by melting in the Peninsula, and greater-than-average melting in the 2022 season was driven by events where low pressure in the southern Bellingshausen Sea combined with high pressure in the Scotia Sea or Falklands delivered warm high-moisture air over the Peninsula, inducing foehn events along the northeastern Peninsula. The pattern was responsible for the 8 February spike in melt (Gorodetskaya et al. 2023) and the earlier December events as well. Considering the rest of the Peninsula, including the George VI and Wilkins ice shelves on the western Peninsula, melt days were on average also 10 to 20 days higher than the reference period (Figs. 6.7a,b). However, melt days on the George VI and Wilkins ice shelves were still less than the exceptional melt season of 2019/20 (Banwell et al. 2021).

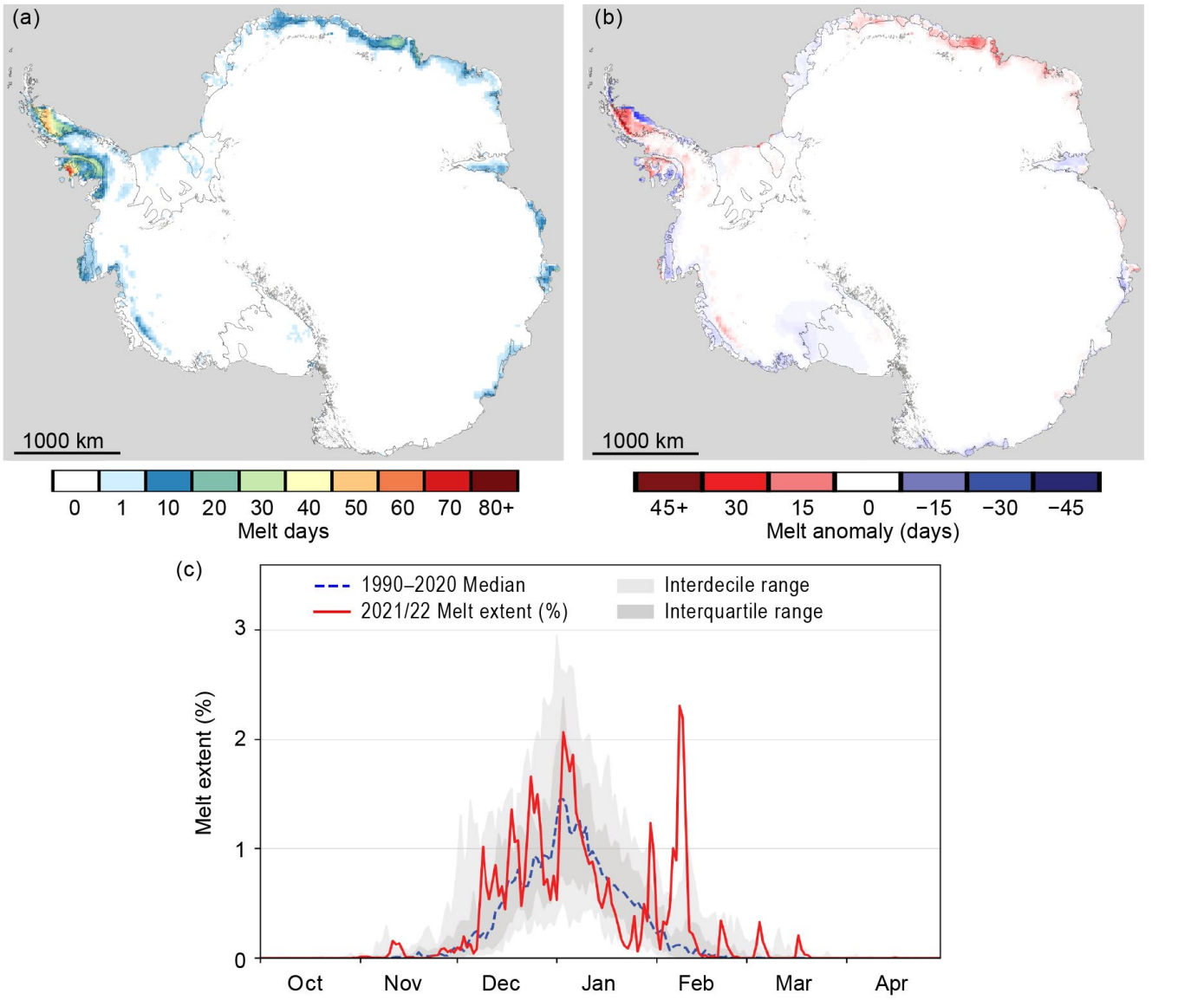

Fig. 6.7. Surface melt across the Antarctic Ice Sheet as detected from passive-microwave satellites. (a) Map of the sum of melt days from 1 Oct 2021–30 Apr 2022. (b) Map of the sum of melt days relative to the 1990–2020 baseline average. (c) Daily melt extent (%, solid red line) compared to median values (dashed blue line), interquartile ranges (dark gray), and inter-decile ranges (light gray) from the 1990–2020 reference period.

The Maud and Enderby regions of Antarctica also displayed a higher-than-average melt season in terms of days, with relatively extensive melt in late December and an extensive melt event in early January that briefly covered nearly 10% of the region's area (Fig. 6.8c). Melt on the Wilkes and Adélie coast of Antarctica typically occurs only on a limited amount of its total land area because of the relatively small area of coastal ice shelves there. Most of the 2021/22 melt season was muted in the Wilkes and Adélie region (Fig. 6.8d), registering nearly no melt with the exception of two extensive melt events in mid-December and mid-March, each of which briefly broke daily melt-extent records in the satellite observational history. The mid-March event was associated with an atmospheric river that caused record-breaking high-temperature anomalies high onto the East Antarctic plateau (see Sidebar 6.1). This event, with a peak extent of 28,100 km^2 on 17 March 2022, broke the observational record during the month of March in Wilkes and Adélie land by 164% (17,100 km^2), and is thus far the most significant late-season melt event recorded in this region later than 4 February in any recorded melt year of the satellite observational record. Most of the remainder of the Antarctic continent saw near-to-below-average melt compared to the reference period, with the Ross Embayment registering nearly no melt for the second consecutive year.

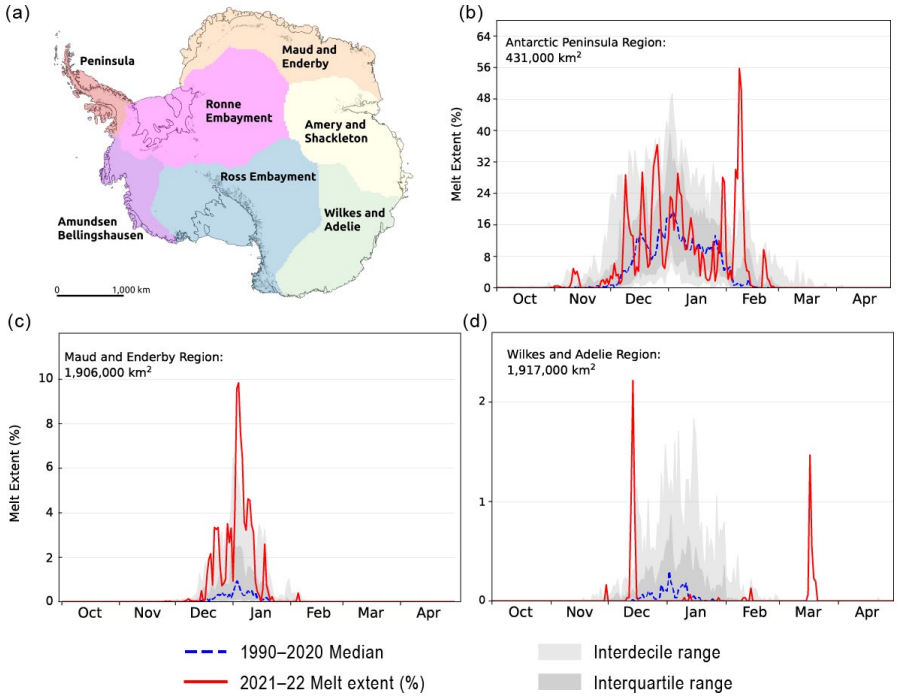

Fig. 6.8. (a) Map of major regions of Antarctica used in regional analyses. (b)–(d) Regional daily melt extents (%) from (b) the Antarctic Peninsula, (c) Maud and Enderby, and (d) Wilkes and Adélie regions.

e. Ice-sheet mass balance

—S. Adusumilli, H. A. Fricker, and A. S. Gardner

The Antarctic Ice Sheet gains mass from accumulation (snowfall minus sublimation) at the surface and primarily loses mass at the margins through its floating extensions, most of which are called ice shelves. Mass loss can occur due to the calving of icebergs at ice shelf fronts, which occurs episodically on multi-annual to multi-decadal time scales, or through continuous ocean-driven basal melting (Rignot et al. 2013; Depoorter et al. 2013; Adusumilli et al. 2020). For any given time period, the net mass balance between competing mass gains and losses depends on the cumulative effects of interactions between the ice, ocean, and atmosphere (e.g., Smith et al. 2020a). Over the past two decades, the ice sheet has experienced net mass loss of grounded ice (e.g., The IMBIE Team 2018), which is in part due to net mass loss of its floating ice shelves (e.g., Paolo et al. 2015) and a corresponding reduction in their "buttressing" effect that otherwise slows the flow of grounded ice into the ocean (e.g., Gudmundsson et al. 2019). Mass loss over the ice sheet has sometimes occurred rapidly in the past (e.g., during the collapse of Larsen B Ice Shelf; Scambos et al. 2004), stressing the need for continuous monitoring through satellite observations.

At the time of writing, there were no published estimates of total Antarctic mass or height change for 2022; however, recent studies (e.g., Smith et al. 2020a) have shown changes in height and mass over the previous decade. The conversion of height changes to mass changes requires a firn density model (e.g., Ligtenberg et al. 2011), which is not yet available for this period. We derived estimates of height changes over the grounded ice sheet from NASA's Ice, Cloud and land Elevation Satellite-2 (ICESat-2) laser altimeter using data for 2022 until the latest available date (12 October 2022). We used the Advanced Topographic Laser Altimeter System (ATLAS)/ICESat-2 ATL06 L3A Land Ice Height data product version 5 (Smith et al. 2020b), which provides precise estimates of height along repeated ground tracks at 20-m along-track resolution. We derived along-track height changes between Cycle 13 (October–December 2021) and Cycle 16/17 (August–October 2022; Fig. 6.9a). To analyze seasonal variability, we also derived height changes over three-month intervals between successive ICESat-2 data acquisition cycles during the October 2021 to October 2022 period (Fig. 6.10). We smoothed the final height change map using a Gaussian filter with a 25-km diameter. We only consider changes in mass over the grounded portion of the ice sheet for the remainder of this study.

For further context, we provide an annual mass change estimate derived from NASA's satellite gravimeter Gravity Recovery and Climate Experiment Follow-on (GRACE-FO; Fig. 6.9b) for 2022. We used data from the Jet Propulsion Laboratory Gravity Recovery and Climate Experiment (GRACE) and GRACE-FO Ocean, Ice, and Hydrology Equivalent Water Height Coastal Resolution Improvement (CRI) Filtered Release 06 Version 03 "mascon data" (Wiese et al. 2023a). Mascons (or mass concentration blocks) are 3° × 3° spherical caps placed on an elliptical approximation of Earth's surface over which these data are provided (Wiese et al. 2023a). We calculated the gravity-derived mass change for November 2021 to November 2022, approximately the same period as used for ICESat-2. To determine ice sheet mass change, we identified all mascons containing more than 10,000 km^2 of land, according to the provided Coastline Resolution Improvement (CRI) land mask. We interpolated the area-averaged rates of change using bilinear interpolation according to the location of the geometric center of the land area contained within the mascon. We then masked all non-land areas using the Bedmachine ice mask (Morlighem et al. 2020). We also show a time series of mass changes integrated over the ice sheet (Fig. 6.10a) from the Level 4 Antarctica Mass Anomaly Time Series data product (Wiese et al. 2023b).

The maps of annual changes in ice-sheet height from ICESat-2 (Fig. 6.9a) and mass from GRACE-FO (Fig. 6.9b) show ongoing losses of ice in the Amundsen Sea sector of West Antarctica,

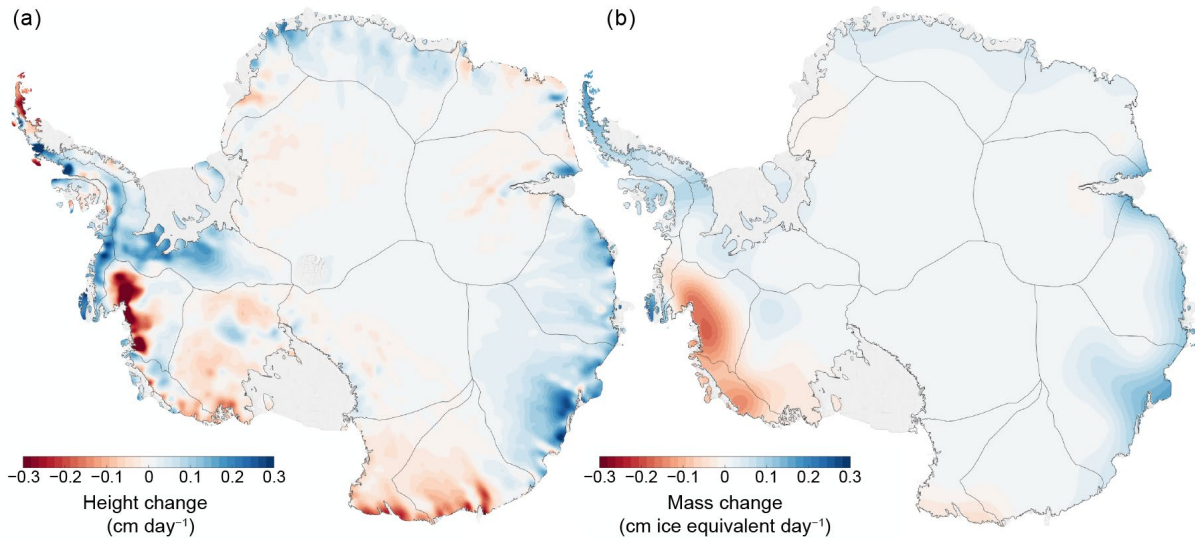

Fig. 6.9. Maps of (a) height change (cm day^{-1}) from ICESat-2 for the Oct 2021–Oct 2022 period and (b) ice equivalent mass change (cm ice equivalent day^{-1}) from GRACE-FO for the Nov 2021–Nov 2022 period.

the same region where losses have been observed over the previous two decades (e.g., Smith et al. 2020a; Clem and Raphael 2022). However, time series of mass changes (Fig. 6.10a) suggest a net mass gain of 290 Gt over the grounded portion of the ice sheet between January 2022 and November 2022, which was unprecedented in the past two decades and substantially different from the average annual mass loss of 120 Gt yr^{-1} between December 2003 and December 2021.

The 2022 surface mass balance anomaly over grounded ice was estimated with reanalysis data to be +325 Gt (see section 6c), which is in line with the GRACE estimate of +290 Gt of mass gain during 2022, combined with the annual average mass loss 120 Gt yr^{-1}. Many of the spatial patterns of increases in height across Antarctica correspond well with patterns of record-high positive surface mass balance anomalies reported in 2022 (see section 6c). For example, large increases in height over Wilkes Land, East Antarctica, during February–May (Fig. 6.10c) coincided with increased frequency of landfalling atmospheric rivers during this period (Fig. 6.6d). This further suggests a major contribution of surface processes in driving seasonal and interannual height and mass changes. Although these increases led to a high positive mass balance signal in 2022, given the exceptional nature of the surface mass gains in 2022 that is unlikely to occur every year, we expect the Antarctic Ice Sheet to revert to its previous state of mass loss in coming years.

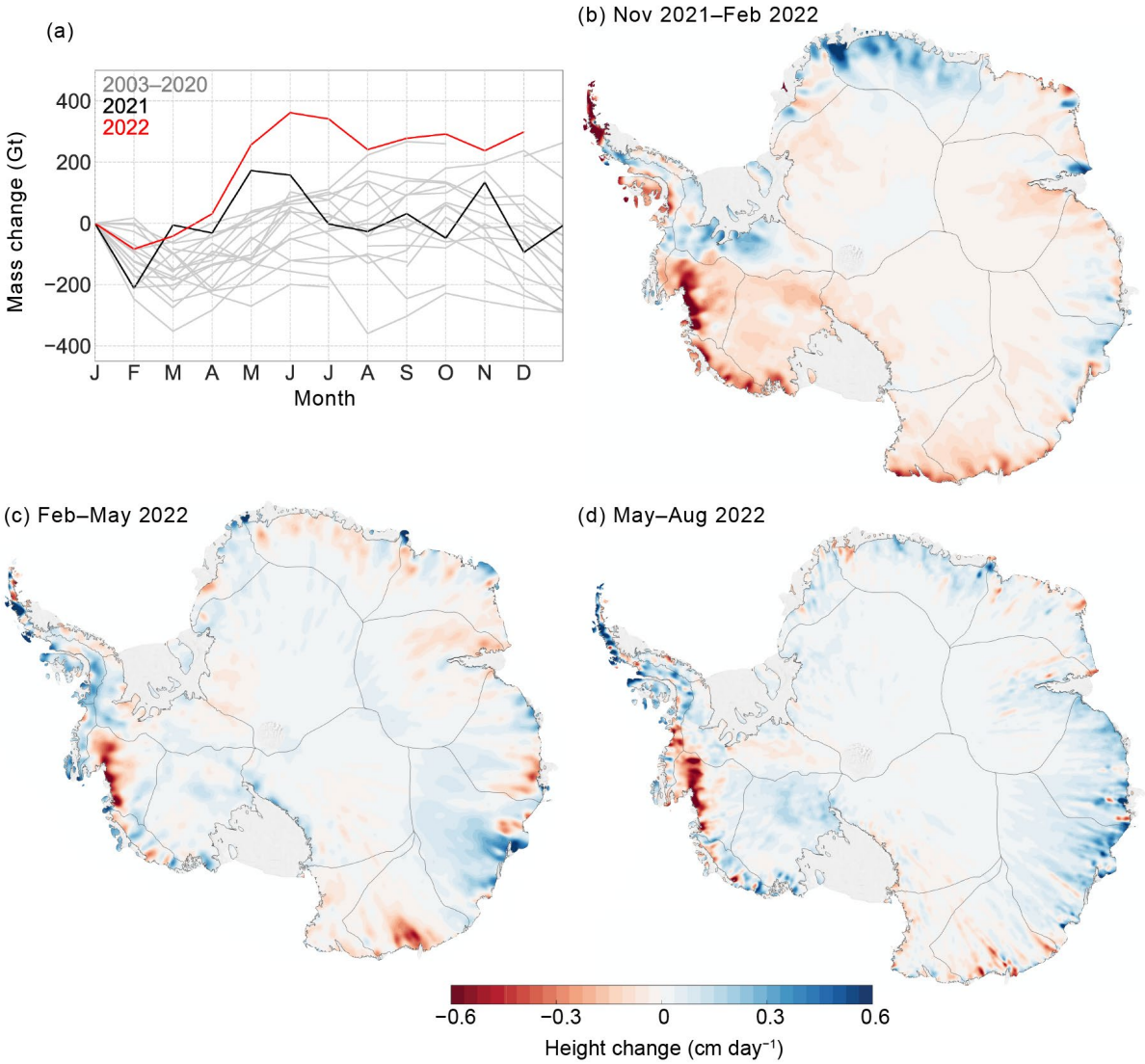

Fig. 6.10. (a) Time series of monthly mass changes from GRACE and GRACE-FO, with 2021 and 2022 highlighted in black and red, respectively. (b)-(d) Maps of height change (cm day^{-1}) from ICESat-2) shown at three-month intervals between Nov 2021 and Aug 2022. Dates represent the central month of each three-month ICESat-2 data acquisition cycle.

f. Sea-ice extent, concentration, and seasonality

—P. Reid, S. Stammerjohn, R. A. Massom, S. Barreira, T. Scambos, and J. L. Lieser

Net sea-ice extent (SIE) and sea-ice area (SIA) were well below or at record-low levels for all of 2022 (based on satellite passive-microwave ice concentration data since 1979 when the near-homogenous satellite record began; Cavalieri et al. 1996). Indeed, there were more than 80 record low daily values of SIE and SIA (Fig. 6.11a, with most occurring during the late 2021/22 retreat and early 2022/23 advance phase (January–March), the wintertime phase (June–September), and the mid 2022/23 retreat phase (December). A new record-low SIE annual

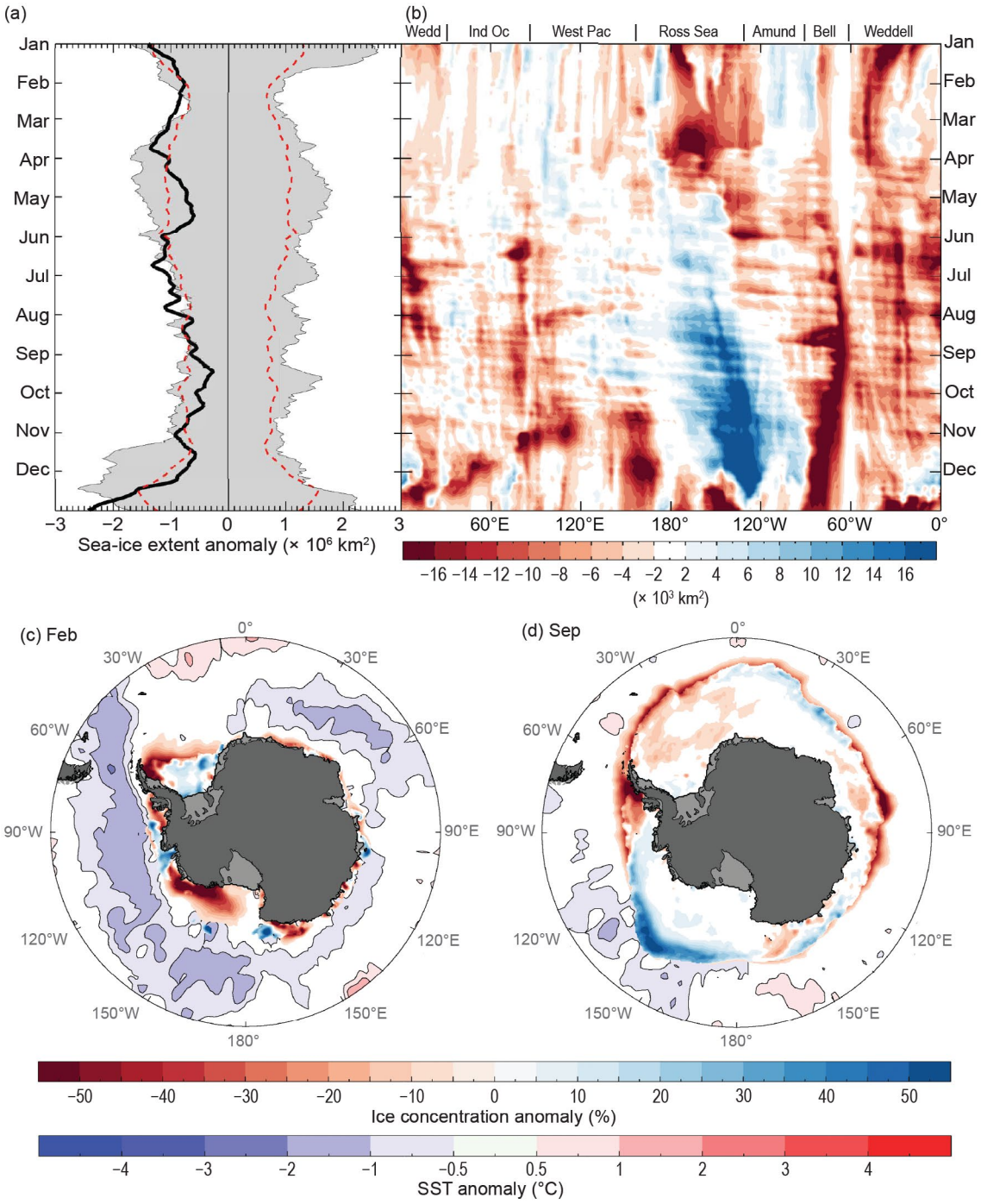

Fig. 6.11. (a) Time series of net daily sea-ice extent (SIE) anomaly for 2022 (solid black line; based on a 1991–2020 climatology). Gray shading represents historical (1979–2020) daily SIE anomaly, red dashed line represents ±2 std. dev., and (b) Hovmöller (time–longitude) representation of daily SIE anomaly (× 10³ km² per degree of longitude) for 2022. Maps of Sea-ice concentration anomaly (%) and sea-surface temperature (SST) anomaly (°C; Reynolds et al. 2002; Smith et al. 2008) for (c) Feb 2022 and (d) Sep 2022. Sea- ice concentration is based on satellite passive-microwave ice concentration data (Cavalieri et al. 1996, updated yearly, for climatology; Maslanik and Stroeve 1999, for the 2022 sea-ice concentration). See Fig. 6.1 for relevant place names.

daily minimum of ~1.96 × 10^6 km^2 was recorded on 25 February (Turner et al. 2022; Wang et al. 2022; NSIDC 2022), breaking the previous record of ~2.08 × 10^6 km^2 on 1 March 2017 (Turner and Comiso 2017; Reid et al. 2018) using the same sea-ice concentration dataset. The annual daily minimum of SIA (~1.25 × 10^6 km^2 on 20 February) was also a record low value, while the 2022 annual daily maximum SIE of ~18.28 × 10^6 km^2 (recorded on 13 September) was the fifth lowest on record. Three months (February, June, and July) observed record-low monthly-mean values of SIE, while there were five months of record-low monthly values of SIA throughout the year. The record-low monthly SIEs continue a recent trend since January 2016, whereby over 85% (72 out of 84) of monthly net SIE values have been below the long-term (1991–2020) average. This reduction in SIE has been most prominent in the late retreat phases (January and February) where net SIE has been below average or at record-low values for every year (2016–22). Fraser et al. (2023) observed record-low values of coastal fast ice area in 2022, along with record-high values of coastal exposure (which refers to the length of coastline without offshore sea ice cover; Reid and Massom 2022). Regionally and after May, the Ross Sea, then Amundsen Sea, experienced generally much greater-than-average SIE, while most other sectors recorded average or lower-than-average SIE throughout the year (Figs. 6.11b,d). Regional and temporal variations are discussed more fully below and closely reflect the three atmospheric phases shown in Figs. 6.2 and 6.3 (see section 6b).

Regional patterns of sea-ice coverage in January–March 2022 largely continued those observed in the latter part of 2021 (Reid et al. 2022), with strong negative SIE anomalies being 1–2 std. dev. below average in the Ross, Bellingshausen, and Weddell Seas (Fig. 6.11b). The negative net SIE anomaly (Fig. 6.11a) at this time was dominated by sea-ice loss in the Ross Sea which saw SIE anomalies of >2 std. dev. below average from late January onward (Fig. 6.11b). This major loss event was driven by wind anomalies associated with an intense and persistent Amundsen Sea Low (ASL; see section 6b, Fig. 6.3a) that had strengthened during September–December 2021 (Fig. 6.3g in Clem et al. 2022), resulting in strong northward ice advection from the Ross Sea into the Amundsen Sea. In the Ross Sea, this contributed to a rapid 2021/22 seasonal retreat (Fig. 6.12b in Reid et al. 2022) followed by persistently low summer sea-ice coverage (Figs. 6.11b,c) with extensive melting of sea ice in the lower latitudes of the northern Ross Sea. The onshore winds associated with the ASL influenced, possibly through melt and/or compaction, the low sea-ice coverage across eastern Bellingshausen and western Weddell Seas during the spring of 2021 and summer of 2022 (Figs. 6.11b,c). During this time, however, greater-than-average sea-ice extent occurred across several less-extensive regions (Figs. 6.11b,c): in the Amundsen and western Bellingshausen Seas (from ~80°W to 120°W) and off Oates Bank (~170°E–180°E), Bunger Hills (~100°E–110°E), and the Amery Ice Shelf (~70°E–80°E). Most of these positive ice anomalies were associated with below-normal sea-surface temperatures to the north of the ice edge (Fig. 6.11c).

In March, initial autumn sea-ice advance was particularly late around most of the continent except for a few coastal areas with small pockets of persistent summer sea ice (centered on 20°W, 90°E, 170°E, 105°W, 80°W; Fig. 6.12a). Seasonal advance was particularly slow in the Ross, western Amundsen, and Bellingshausen Seas where persistent and strong cyclonic activity occurred from January to March (see Fig. 6.3a) and in most of the Weddell Sea with relatively warm northerly flow on the eastern side of the ASL. In addition, as elsewhere, the reduced/delayed sea-ice formation was coincident with the presence of slightly above-average surface water temperatures (see section 6g) possibly as a result of a combination of enhanced solar heating and upwelling.

The unprecedented East Antarctic "heatwave" event on 17–18 March (see Sidebar 6.1) did not initially impact on the large-scale sea-ice pattern off Wilkes Land (the heatwave epicenter). Rather, on 21 March a distinct SIE anomaly was observed farther to the west, off the Amery Ice Shelf, possibly as the abnormal heat became entrained in a subsequent low-pressure system, reducing SIE in that region (Fig. 6.11b) and delaying sea-ice advance (Fig. 6.12a).

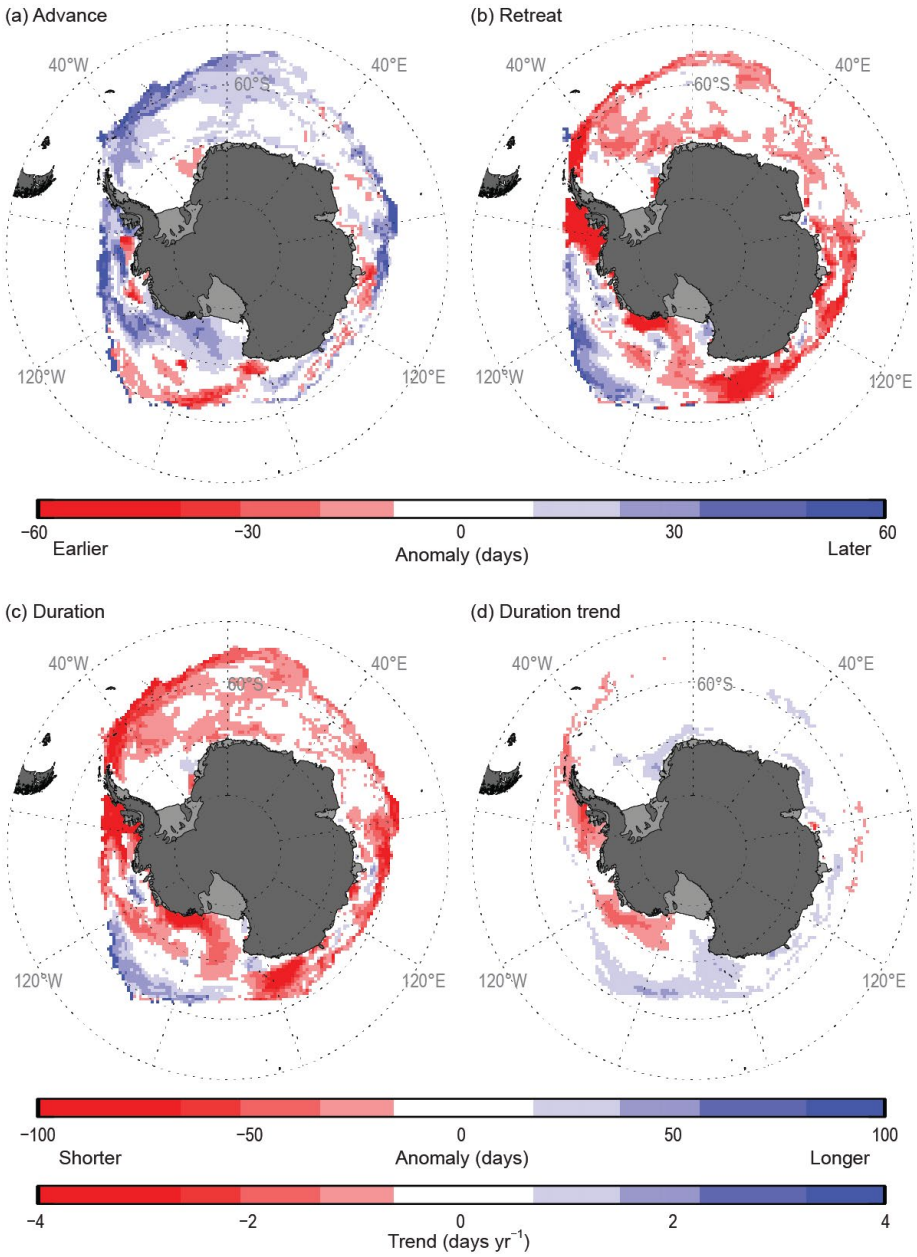

Fig. 6.12. Maps of seasonal sea-ice anomaly (days) in 2022 during (a) autumn ice-edge advance, (b) spring ice-edge retreat, and (c) winter ice season duration; together with (d) winter ice season duration trend (days yr^{-1}; Stammerjohn et al. 2008). The seasonal anomalies (a)–(c) are computed against the 1991/92 to 2020/21 climatology; the trend (d) is computed over 1979/80–2022/23. The climatology (for computing the anomalies) is based on data from Comiso (2017; updated yearly), while the 2022/23 ice-edge retreat duration-year data are from the NASA Team NRTSI dataset (Maslanik and Stroeve 1999); the trend is based on the merged dataset containing 1979-2021 data from Comiso (2017) and 2022/23 data from the NASA Team NRTSI dataset (Maslanik & Stroeve, 1999).

During April–October, the ASL both persisted and deepened (see Fig. 6.3c; especially in April–May and August–September, not shown), with relatively benign atmospheric conditions around the rest of the continent. Hence, annual sea-ice advance continued to be later than usual around most of the continent (Fig. 6.11b), the exception being around ~100°E–110°E (Bunger Hills) where the sea ice had not fully retreated in the previous year and subsequently advanced earlier than usual (shown in blue, Fig. 6.11b and in red, Fig. 6.12a). This region then had greater-than-average SIE through the end of May. Of some prominence is a pattern from May onward of an ice advance recovery in the outer Ross Sea (Fig. 6.11b), with a substantially higher-than-average SIE from mid-May onward that intensified at the beginning of August

(through early December). This was again consistent with the unusual persistence of a strong ASL (see Figs. 6.3c,e), which drew colder air seaward off the continent to enhance both northward sea-ice advection and freezing conditions over the Ross Sea. During this time, SIE within the Ross Sea was generally 1–2 std. dev., but as much as 2–4 std. dev., above average.

Elsewhere and from April through October, SIE was considerably lower than normal, with two regions being exceptionally low. The first is the Amery region (~60°E–100°E), an area across which transient cyclones are preferentially steered and then stalled by a strong blocking high to the east during this period (see Fig. 6.3c). One particularly deep cyclone on about 9 June caused a relatively rapid sea-ice retreat within the Amery region (leading to a SIE of >4 std. dev. below average for a few days), and localized SIE remained substantially lower than average through the end of 2022 (Fig. 6.11b). The second region that saw below-average SIE from April through October was the Bellingshausen-western Weddell Seas sector (~80°W–10°E). There, the persistence and eastward migration of the intense ASL maintained warm northerly winds, which substantially delayed or minimized ice advance and/or formation, leading to below-average SIE. For the region ~80°W–40°W, sea ice retreated early (Fig. 6.11b), exposing much of the far southwestern Peninsula and Eights Coast to open-ocean (sea ice-free) conditions. Hence during September when net SIE reached its annual maximum, only the Ross and Amundsen Seas had positive SIE anomalies (Figs. 6.11b,d). The September sea-ice concentration anomalies (Fig. 6.11d) further reflect the synoptic-scale effects of the repeat passage of transient cyclones across the Amundsen Sea (facilitating ice-edge expansion through divergence) and their subsequent stalling and weakening in the Bellingshausen Sea, causing warmer conditions and ice-edge compaction.

During November–December, the ASL remained stronger than average, combined with an overall intensification and southward contraction of the circumpolar low-pressure trough that was especially deep across much of East Antarctica (see Fig. 6.3e)—a pattern reflecting a strong positive Southern Annular Mode (SAM). Resultant increased cyclonic activity around maritime East Antarctica led to a rapid seasonal (late spring-early summer) sea-ice retreat and strongly negative SIE anomalies in this sector (of up to 2–4 std. dev. below average in some regions) i.e., the Amery region (~70°E–90°E) in early November and Adélie Land (~140°E–170°E) during most of December (Fig. 6.11b). In November, sea ice continued to retreat rapidly in many sectors, notably east of 80°E and particularly from 130°E to 170°E, as well as in the southeastern Ross Sea from 120°W to 180°W (Fig. 6.12b). In stark contrast, and as was the case in the early austral summer of 2021, strong northward sea-ice advection to warmer low latitudes maintained substantially higher-than-average SIE in the eastern Ross Sea to western Bellingshausen Sea (90°W–160°W) that persisted well into mid- to late-December (early summer), after which an abrupt switch to rapid recession/melting occurred (Fig. 6.11b). These rapid sea-ice retreat anomalies (Fig. 6.12b), coupled with the preceding slow sea-ice advance anomalies (Fig. 6.12a), resulted in anomalously short sea-ice seasons (duration) for most Antarctic sectors, with the exception of 120°W–170°W (Fig. 6.12c). The substantially short ice-season duration in the eastern Bellingshausen Sea (60°W–80°W) and western Amundsen/eastern Ross Seas (120°W–160°W) reinforce the strong negative ice-season duration trends observed over 1979/80–2022/23 (Fig. 6.12d). Similarly, the longer ice-season duration anomalies in the outer western Amundsen/eastern Ross Seas sector reinforce the positive ice-season duration trends observed there. Elsewhere, the 2022 ice-season anomalies stand in contrast to the 1979/80–2022/23 ice-season trend pattern.

Placing 2022 into longer-term context, the continuation in 2022 (and 2023 as of this writing, which will be discussed in next year's report) of a major negative net SIE trend that began in September 2016—and that abruptly followed on from successive record-high Antarctic SIE maxima in 2013 and 2014 (Reid and Massom 2015)—raises an important issue as to whether a major shift has occurred in Antarctica's tightly coupled sea ice–ocean–atmosphere–ice sheet system. Turner et al. (2017) attributed the sudden initial transition from near-record-high SIE to consistently below-average extents to a period of weak circumpolar winds and several strong cyclones that ushered in both warm air and warmer surface waters. However, the circumpolar

westerlies were stronger than average for most of 2021 and 2022 when new record-low SIE values have occurred (see section 6b). The persistently low net SIE since 2017 has since been attributed to a combination of long-term ocean and springtime atmospheric warming (Eayrs et al. 2021). Zhang et al. (2022) show that since 2016 the subsurface of the Southern Ocean has had a more dominant influence in driving the negative Antarctic SIE anomaly in comparison to atmospheric forcing. Similarly, Hobbs et al. (2023, manuscript submitted to *J. Climate*) show that recent summertime sea-ice variability has been largely influenced by the notable lack of ice coverage in the Amundsen and Bellingshausen Seas, such that net summer SIE in recent years has been determined by sea-ice variability in the Weddell Sea and hence has a weaker relationship to major large-scale climate modes such as the SAM. To some degree, apart from the very high SIE in the outer Ross and eastern Amundsen Seas due to a persistently deep ASL, the pan-Antarctic SIE (Figs. 6.11b–d) and ice season (Figs. 6.12a–c) anomalies observed in 2022 were unusually widespread and circumpolar as highlighted in Liu et al. (2023) and Hobbs et al. (2023, manuscript submitted to *J. Climate*).

There are major potential implications for a persistently low sea-ice cover. These include changes in continental snow accumulation (Wang et al. 2020), including: the potential that the low sea-ice cover in 2022 may have contributed to the record-high surface mass balance and ice-sheet mass balance in 2022; increased coastal air temperature; exposure of fast ice and ice-shelf fronts to longer periods of open water and wave action (see Sidebar 6.2; Massom et al. 2018; Teder et al. 2022); changes in deep water and bottom water formation (and hence ocean circulation and temperature); and the potential for greater bioactivity due to increased open-water fraction during warmer months.

Sidebar 6.2: **Larsen B fast-ice breakout and initial glacier response**

—N. OCHWAT, A. BANWELL, AND T. SCAMBOS

Since the disintegrations of the Larsen A and Larsen B ice shelves in 1995 and 2002, respectively, landfast sea ice (stationary and consolidated sea ice that is attached to the coastline, hereafter 'fast ice') has formed in the areas previously occupied by these ice shelves. For the Larsen A, this fast ice has broken out nearly every summer since the ice shelf's collapse. For several years following the collapse of the Larsen B, fast ice in the embayment was also generally absent by February. However, in late March 2011, fast ice formed in the Larsen B embayment and remained continuously for the next 11 years. The tributary glaciers along the Larsen B coast advanced several kilometers into this fast ice during the 11-year occupation, forming extensive glacial ice tongues that compressed and rifted the adjacent fast ice. On 20 January 2022, the fast ice abruptly fractured throughout its extent, following small calving events during 17–19 January (Figs. SB6.4a–c). By 8 February, the embayment was almost completely clear of broken sea-ice floes. Concurrent with the break-out of the ice, the Larsen B glaciers in the embayment began a rapid retreat as the ice tongues calved rapidly into large tabular blocks and smaller calved ice debris, as shown in a series of aerial photos of the ice front areas and the mélange acquired by the British Antarctic Survey on 31 January 2022 (Fig. SB6.4d).

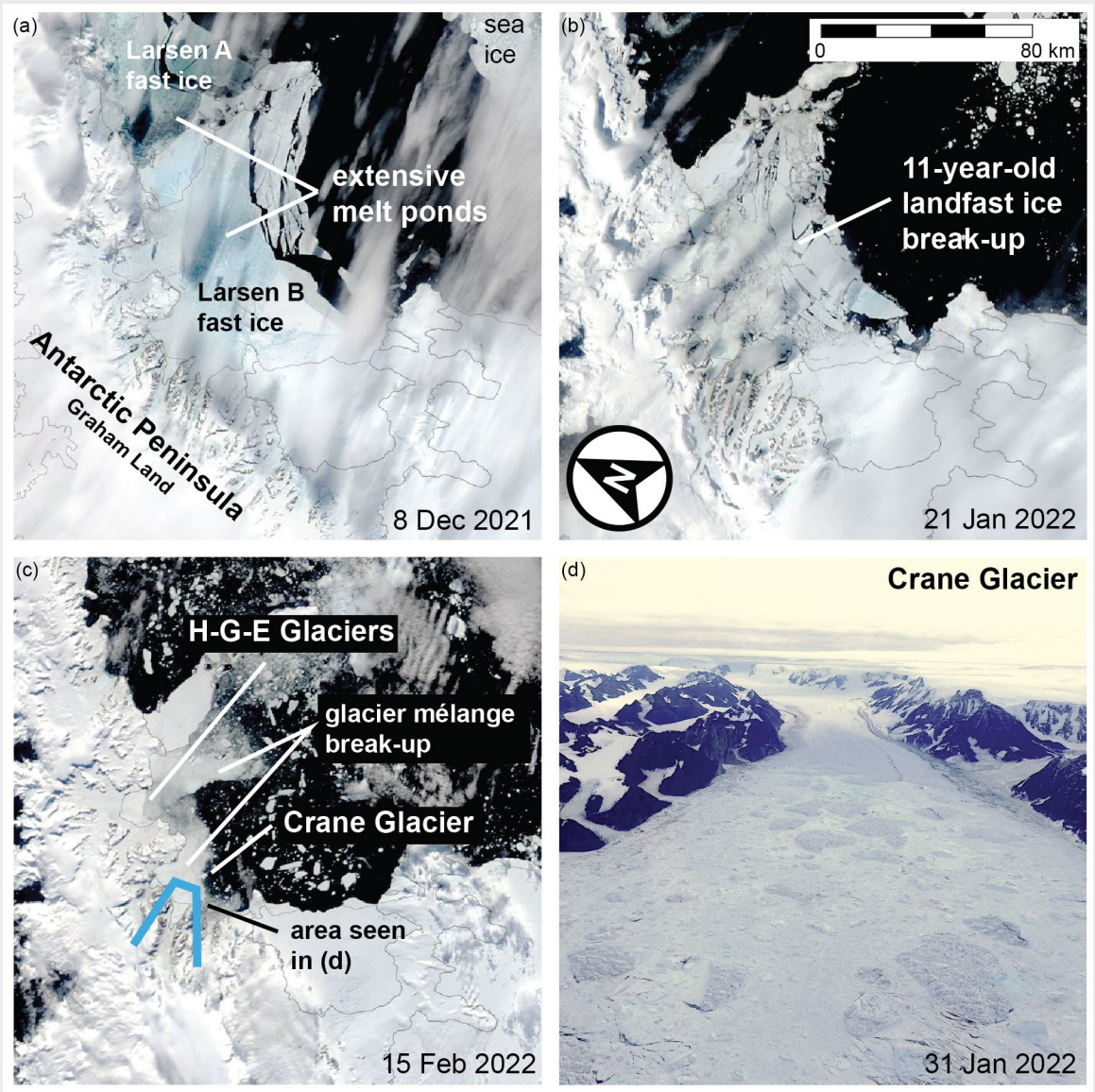

Fig. SB6.4. (a)–(c) Landsat 8 true-color images of the Larsen A and Larsen B embayments spanning the period of the breakup of the 11-year-old Larsen B fast ice. (d) Enhanced-color hand-held aerial photograph of the Crane Glacier fjord looking southwestward, acquired by British Antarctic Survey.

The cause of the fast-ice breakout appears to be a combination of warm summer air temperatures and wave action. Intense surface melting occurred in the region in the 2021/22 summer (https://nsidc.org/greenland-today/2022/02/) that likely pre-conditioned the fast ice cover for breakup, but intense surface melting and flooding of the fast ice by meltwater had happened before, particularly in 2015/16 and 2019/20 (e.g., Banwell et al. 2021, see their Fig. 2; Bevan et al. 2020; by inference of extensive melting in the northern Larsen C). However, unlike previous summers, sea ice in the adjacent northwestern Weddell Sea was greatly reduced in 2021/22 (Figs. SB6.5a,b). Sea-ice pack, even at relatively low concentrations, sharply dampens surface ocean waves within a few kilometers of the sea-ice front (Squire et al. 1995; Zhao et al. 2015). In early January 2022, for the first time in the 2011–22 fast ice period, a ~50 km-wide ice-free corridor (concentration below 15%) opened in the northwestern Weddell Sea, facilitating ocean swell penetration to the Larsen B fast-ice front. Examining both WAVEWATCH III (Tolman 2009) and European Centre for Medium-Range Weather Forecasts Reanalysis version 5 (ERA5) wave data (Hersbach et al. 2020; not shown), the first large swell able to reach the Larsen B fast ice edge occurred on 18–19 January (Fig. SB6.5c), with an estimated peak amplitude of 1.75 m and a peak wave period of 5 s (equal to a wavelength of ~40 m). Wave propagation direction was bearing ~250°±25° through this period, similar to the orientation of the open corridor in the sea ice. Our analysis looked at wave data grid cells adjacent to the Larsen B fast ice front as well as cells ~150 km to the northeast near James Ross Island (Fig. SB6.5c). Subsequent foehn events, triggered by atmospheric rivers impacting the western flank of the Peninsula (e.g., 20 January, 29–30 January, and 7–9 February), cleared the broken ice and much of the mélange of ice blocks and rafted thick sea ice from the embayment as a rapid up-fjord retreat of the ice tongues progressed.

Fast ice has been shown to have a stabilizing effect on ice shelves and glaciers, and its loss is frequently associated with ice-shelf breakup or glacier retreat (Massom et al. 2010, 2018; Gomez-Fell et al. 2022; Fraser et al. 2023). After the Larsen B Ice Shelf collapsed in 2002, glaciers that formerly flowed into the ice shelf calved and retreated rapidly. However, over the 11-year period of fast-ice presence, the Larsen B glaciers partially re-advanced, protected from wave action and supported by backstress from the fast ice in the bay (notably Crane and Jorum glaciers, and the Hektoria-Green-Evans glacier system).

With the break-out of the fast ice in early 2022, these glacier tongues, mélange areas, and in some cases previously grounded ice retreated and collapsed. Unlike previous winter seasons, fast ice did not form in the embayment in the 2022 winter. The pack ice in the embayment remained

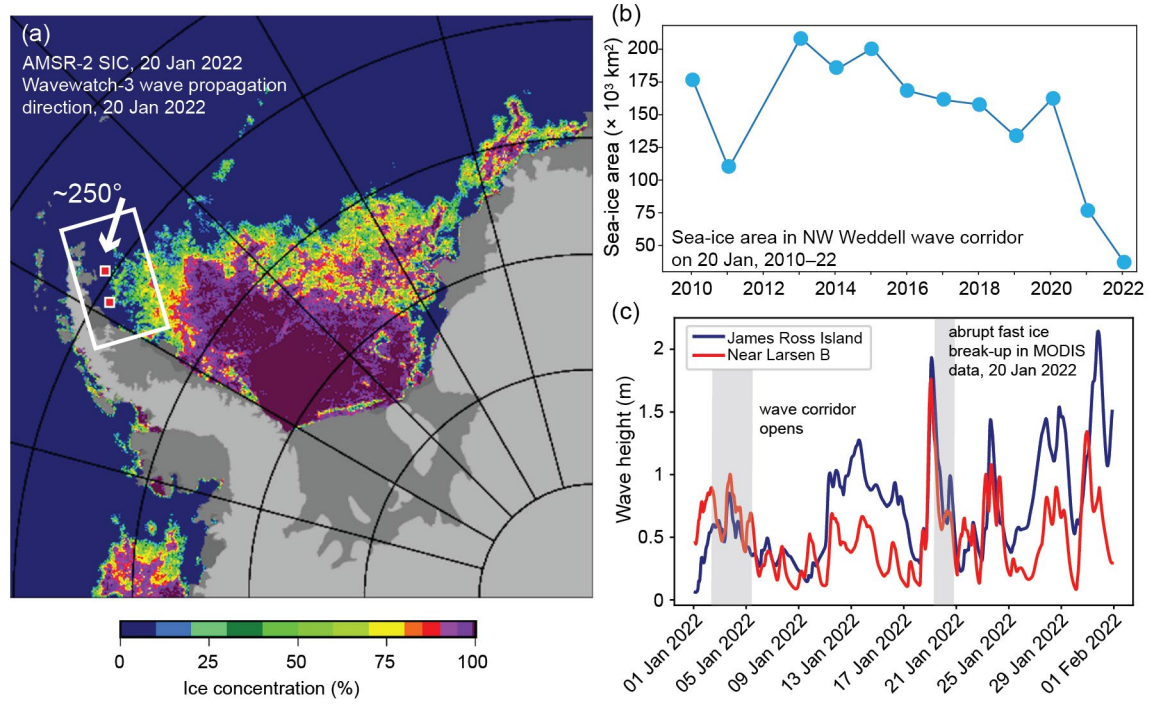

Fig. SB6.5. (a) Sea-ice conditions on 20 Jan 2022, showing ice concentration (%) and distribution from AMSR-2 data (Spreen et al. 2008; https://seaice.uni-bremen.de/sea-ice-concentration/amsre-amsr2). Wave propagation direction on 20 Jan from Wavewatch-3 data is shown by the white arrow (~250° true); white outline shows the region assessed for sea-ice area in (b); red squares show the location of the Wavewatch-3 wave height grid cells shown in (c); (b) sea ice area (10^3 km^2) from AMSR and AMSR-2 data in the corridor region of the northwest (NW) Weddell Sea for 2010–22; (c) wave height data (m) for Jan (starting at 0000 UTC on 1 January 2022) from ERA5 Wavewatch-3 gridded wave timeseries for the grid cell areas in (a).

mobile and strong foehn wind events (e.g., 20–23 September) repeatedly cleared the ice from the glacier fronts. By the end of 2022, Crane Glacier had lost ~10 km of floating ice, and the ice front was at or slightly above the most upstream location ever observed (see Shuman et al. 2011). The Hektoria-Green-Evans system collapsed upstream a total of ~26 km, and the merged trunk for the three glaciers disintegrated. The collapse event is similar to the rapid evolution of the Röhss Glacier on James Ross Island in the years following the Prince Gustav Ice Shelf disintegration (Glasser et al. 2011).

The stark change in fast-ice stability as the fringing sea-ice pack dispersed timed closely to the arrival of a significant ocean wave train, and the rapid evolution of the former tributary glaciers in response to fast-ice loss, point to the potential impacts on ice-sheet stability and mass balance change that arise if the current downward trend in summer Antarctic sea-ice extent continues. The events point to a clear connection between late-summer wave flexure of warm, melt-laden fast ice, and significant glacier destabilization in areas where long-term fast ice is removed by wave action.

g. Southern Ocean

—L. Pezzi, R. Beadling, M. du Plessis, S. Gille, S. A. Josey, J.-R. Shi, M. Santini, E. Souza, G. MacGilchrist, and C. Schultz

The Southern Ocean (SO) has an important role in Earth's global climate. It is a significant sink for anthropogenic CO_2 and heat (Gille 2002; Frölicher et al. 2015; Shi et al. 2018) and is the world's most biologically productive ocean (Liu and Curry 2010). The SO is changing rapidly, exhibiting significant warming to the north of the Antarctic Circumpolar Current (ACC; Armour et al. 2016; Sallée 2018; Shi et al. 2021), as well as freshening (Swart et al. 2018) and decreasing oxygen (Shepherd et al. 2017). Here we analyze 2022 anomalies of SO sea-surface temperature (SST), surface salinity, mixed layer properties, air–sea heat fluxes, ocean heat content (OHC), surface chlorophyll, and oxygen concentrations. For surface chlorophyll and oxygen, we focus on austral spring 2021 and summer 2021/22 to highlight the phytoplankton growth season.

1. SEA-SURFACE AND MIXED-LAYER PROPERTIES

We present 2022 SO SST anomalies relative to the 1991–2020 climatology computed from the NOAA Optimum Interpolation SST version 2 product (Reynolds et al. 2002). The 2022 SO surface salinity and mixed layer depth (MLD) anomalies are relative to 2005–20 climatology and also presented (Figs. 6.13b,c), with data from the Argo-based dataset from Roemmich and Gilson (2009; RG09). The depth at which potential density referenced to the surface changes by 0.03 kg m^{-3} relative to potential density at 10 m (de Boyer Montégut et al. 2004) is used to define MLD. MLD anomalies are computed relative to a 2004–21 climatology. Following Beadling et al. (2022), we focus on 40°S–65°S since this region encapsulates SO climatic variability and the ACC.

Annually averaged SSTs in 2022 (Fig. 6.13a) were mostly below average, between −0.5°C and −1.5°C across much of the west and east Pacific, between −0.15°C and −0.5°C in the western Indian, and between −0.15°C and −0.5°C in the western Atlantic at the Drake Passage. With the exception of the Atlantic, the greatest negative SST anomalies were generally found south of the subantarctic front (SAF), while positive SST anomalies characterized regions farther north of the SAF, with particularly strong positive SST anomalies north of 40°S in the South Pacific. Most of the Atlantic sector of the SO was warmer than usual.

The anomalously high SSTs in the Atlantic and Indian sectors resulted in a net positive SST anomaly for the SO in 2022 (Fig. 6.13d), following the warming tendency shown in Beadling et al. (2022). Regions with the highest SST coincided with positive sea-surface salinity anomalies (Fig. 6.13b). Between the SAF and Southern Boundary Front in the South Pacific, positive surface salinity anomalies co-occurred with anomalous cooling. Positive surface salinity anomalies were observed in all oceans starting in April 2022 (Fig. 6.13e). The SO MLD reveals anomalously

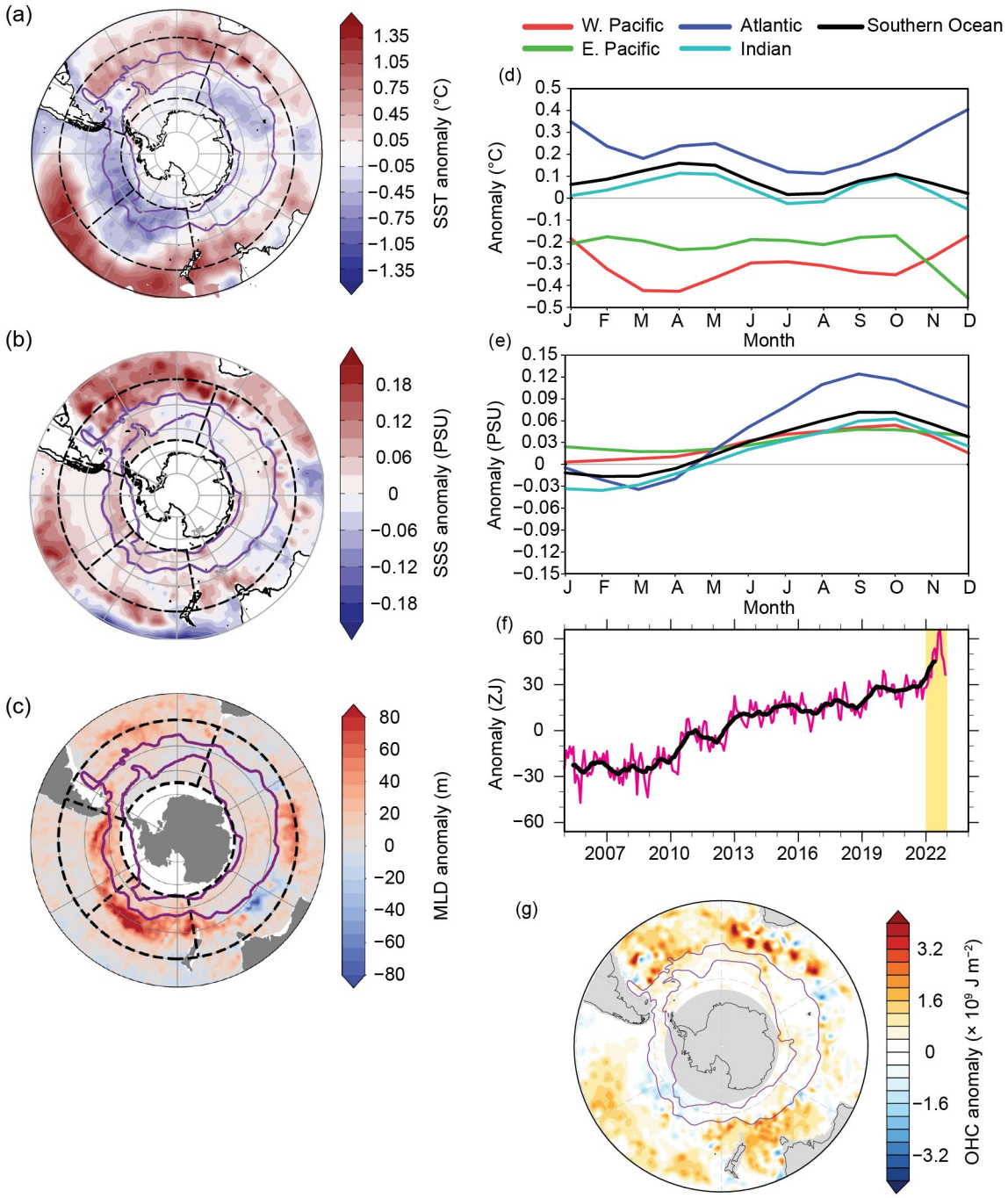

Fig. 6.13. 2022 annual average (a) sea-surface temperature (SST; °C), (b) surface salinity (SSS) (PSU), and (c) mixed layer depth (MLD; m) anomalies. Time series of monthly average (d) SST and (e) surface salinity anomalies. (f) Time series of monthly average of upper-2000-m ocean heat content (OHC) anomaly (ZJ or 10^{21} J) relative to 2005–20 Argo climatology south of 30°S (pink curve) with 12-month running mean on top (black curve) and 2022 highlighted in yellow shading. (g) Map of 2022 OHC anomalies (× 10^9 J m^{-2}). SST anomalies are computed relative to a 1991–2020 climatology, while surface salinity, OHC, and MLD use a 2004–21 climatology given the limited extent of the RG09 product. Purple contours in the maps indicate the location of the subantarctic and southern boundary Antarctic Circumpolar Current fronts as defined by Orsi et al. (1995). Four distinct regions between 40°S and 65° are delineated by black dashed contours in Figs. 6.13a–c, corresponding to the western Pacific (170°W–120°W), eastern Pacific (120°W–70°W), Atlantic (70°W–20°E), and Indian (20°E–170°E) sectors discussed in the text.

deep mixing in the South Pacific just north of the SAF (Fig. 6.14c), similar to 2021 (Beadling et al. 2022). However, the deepest mixing was centered in the east Pacific sector in 2021 and migrated to the west Pacific in 2022. Deeper MLDs were found north of the SAF in the Atlantic and Indian sectors in 2022 relative to 2021.

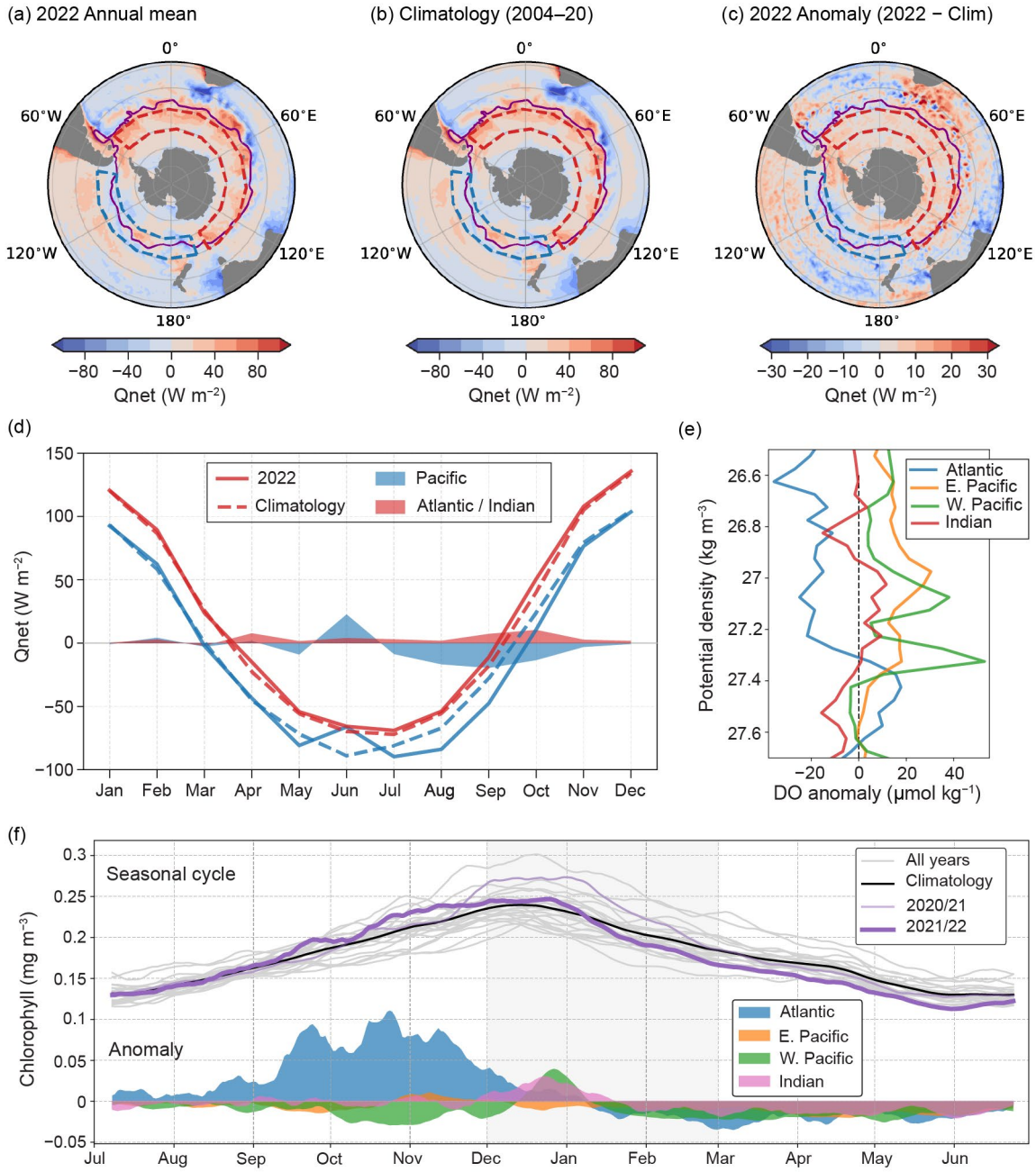

Fig. 6.14. ERA5 net heat flux, Qnet (W m^{-2}): (a) 2022 annual mean, (b) 2004–20 climatology, and (c) 2022 anomaly. The purple line denotes the location of the Subantarctic Front as in Fig. 6.13. The blue and red boxes indicate the Pacific (50°S–60°S, 160°E–80°W) and Atlantic/Indian (50°S–60°S, 50°W–150°E) sectors, respectively, chosen for further analysis. Positive values indicate the ocean heat gain. (d) Monthly mean net surface heat flux (W m^{-2}) for the Pacific (blue line) and Atlantic/Indian (red line) sectors of the Southern Ocean during 2022 (dashed) and the 2004–20 climatology (solid). Shading shows the 2022 anomaly from the climatology. (e) Jul 2021–Jun 2022 dissolved oxygen anomalies (kg m^{-3}) relative to the 2005–20 Argo climatology. Potential density was calculated from pressure, temperature, and salinity data, and binned into 0.05 kg m^{-3} intervals. (f) Seasonal cycle of the area-weighted (40°S–65°S), daily mean chlorophyll concentration (mg m^{-3}): all historical years (gray lines); the climatological mean for 1997–2022 (black line); the most recent two growing seasons (purple lines); anomalies relative to climatological mean for each basin (colored shading). A 14-day rolling average was applied to all time series. The x-axis is centered on the austral summer months. (Source: data are derived from the multi-satellite merged, cloud-free product; https://doi.org/10.48670/moi-00281.)

2. UPPER-OCEAN HEAT CONTENT

Monthly gridded temperature data from RG09 were used to evaluate 0-m–2000-m SO OHC anomalies relative to the 2005–20 climatological seasonal cycle. We focus on 30°S–65°S since a substantial OHC increase occurred in this region (Shi et al. 2021). In 2022, the SO annual mean upper-2000-m OHC anomaly increased by 16.2 ZJ (10^{21} J) to +45.2 ZJ (Fig. 6.13f) This increase in OHC is much larger than the increase between 2020 and 2021 (2.5 ZJ; Clem et al. 2022) and much larger than the interannual variability (5.2 ZJ south of 30°S) estimated from 1 std. dev. of the detrended annual OHC during 2005–20. The long-term positive trend in SO OHC is more apparent and larger in 2022 (+3.97 ZJ yr^{-1} during 2005–22 versus +3.68 ZJ yr^{-1} during 2005–21). This continuous heat gain is consistent with the 2022 OHC increase (Cheng et al. 2023). However, for the SO, a tremendous austral winter warming occurred in 2022 that was not clearly shown in Cheng et al. (2023).

Consistent with previous studies, most of the enhanced OHC occurred north of the ACC, with pronounced positive anomalies in the South Atlantic, Agulhas Return Current, South Pacific to the north of 50°S, and southwest Pacific around western boundary currents (Fig. 6.13g). The OHC anomalies are smaller within and south of the ACC associated with upwelling of deep water. Although they are smaller in magnitude compared with the lower-latitude anomalies, these positive anomalies can be found around the Antarctic, except for the negative anomalies in the vicinity of the Pacific Antarctic Ridge.

3. AIR–SEA HEAT FLUXES

The European Centre for Medium-Range Weather Forecasts Reanalysis version 5 (ERA5) is used to evaluate the 2022 and 2004–20 climatological state of the surface net heat flux for the Southern Ocean (Hersbach et al. 2020). Air–sea heat fluxes in 2022 showed asymmetrical patterns of anomalies relative to the 2004–20 climatology (Figs. 6.14a,b). This is consistent with previous work (Song 2020; Tamsitt et al. 2020; Josey et al. 2023). In both 2022 and the climatology, the Atlantic and Indian sectors showed a large spread in positive heat flux (ocean heat gain) of 20 W m^{-2} to 80 W m^{-2}. In comparison, the Pacific sector along the ACC experienced large regions of negative heat flux (ocean heat loss) down to –40 W m^{-2}, largely within and surrounding the SAF. Further heat loss was observed within the continental shelf regions surrounding Antarctica.

This zonal asymmetry was further amplified in 2022, with heat fluxes in the Atlantic and Indian sectors consistently higher than the climatology by up to 20 W m^{-2} and the Pacific regions around and south of the SAF experiencing negative heat fluxes as low as –15 W m^{-2} (Fig. 6.14c).

To elucidate potential mechanisms defining the seasonal cycle of heat-flux variability, we investigate the monthly average heat flux in regional boxes in the Atlantic and Indian sectors (50°S–60°S, 50°W–150°E) and the Pacific sector (50°S–60°S, 160°E–80°W) as defined in the zonal asymmetry analysis of Josey et al. (2023). The monthly mean heat flux revealed that the largest zonal asymmetry was observed in summer (December–February) at ~25 W m^{-2} and the lowest in winter (June–August) at ~10 W m^{-2} (Fig. 6.14d). Compared to the 2004–20 climatology, the 2022 annually averaged heat flux anomaly of the Atlantic/Indian sector was +3.5±3.3 W m^{-2} (Fig. 6.14d). This contrasted with the Pacific sector, where large monthly mean heat loss anomalies in winter/spring (reaching a most negative value of –19.5 W m^{-2} in September) led to an overall 2022 heat flux anomaly of –3.9±10.7 W m^{-2}. The large monthly variability in the 2022 heat flux in the Pacific (most notably in June, which had heat gain rather than loss) may be due to variations in the number of episodic heat loss events as previously observed south of Australia (Ogle et al. 2018; Tamsitt et al. 2020). Additionally, Pacific heat loss in 2022 coincided with lower SSTs, deeper MLDs, and a decrease in the OHC (Fig. 6.13), suggesting a potential seasonal response time between heat flux, surface temperature, and mixing. However, further investigation is required to establish whether this was the case.

4. OCEAN BIOGEOCHEMISTRY

We present anomalies of dissolved oxygen (DO) relative to the 2005–20 Argo climatology and satellite-observed chlorophyll concentrations relative to the 1997–2022 climatological mean (Figs. 6.14e,f). For the DO anomalies, data from Argo floats that sampled each region were averaged for the period considered (July 2021–June 2022) and compared to the average DO from all Argo floats available in previous years, starting in 2005. Anomalous conditions were observed in satellite-observed chlorophyll and float-observed oxygen levels during 2021/22, particularly in the Atlantic sector. Mean chlorophyll concentrations were anomalously high during the spring and early summer growing season (Fig. 6.14f, thick purple line) before dropping below climatological levels by mid-January and reaching some of their lowest recorded levels by the onset of autumn. A basin breakdown of anomalies reveals that this pattern arose almost entirely from the Atlantic sector. Mean concentrations between +0.05 and +0.10 mg m^{-3} above climatological levels were seen throughout spring, reaching a maximum in mid-October, before a precipitous decline. By mid-summer, concentrations were anomalously low, indicating an early phytoplankton bloom cycle. In the Pacific and Indian Oceans, chlorophyll concentrations were anomalously low through 2021/22, with the exception of a spike during December and early January in the Pacific.

As with chlorophyll, there were distinct patterns in DO concentrations in the Atlantic relative to other sectors of the SO, with lighter water masses (ρ_0<27.4 kg m^{-3}) exhibiting anomalously low concentrations (Fig. 6.14e). A distinct pattern between the Atlantic and other ocean basins is somewhat consistent with the other metrics shown here. In particular, there is evidence that the positive MLD, surface temperature, and heat flux anomalies are weaker in the Atlantic compared to the Pacific basin. The different observational periods between metrics—where it is more intuitive for biogeochemical metrics to center the annual cycle around the growing season—make it challenging to ascertain what drove the anomalous Atlantic basin conditions in late 2021.

h. 2022 Antarctic ozone hole

—N. A. Kramarova, P. A. Newman, E. R. Nash, S. E. Strahan, B. Johnson, M. Pitts, M. L. Santee, I. Petropavlovskikh, L. Coy, and J. D. Laat

The 2022 Antarctic ozone hole was the 18th largest in 43 years of satellite observations since 1979, with an average area of 21.6 × 10^6 km^2 (averaged for 7 September–13 October) and a minimum daily total ozone column of 97 DU on 1 and 2 October. The meteorological conditions and seasonal development of the Antarctic ozone hole in 2022 were similar to those observed in 2020 and 2021. Following the August–September depletion phase, the 2022 ozone hole persisted, breaking up on 16 December (the 1990–2022 average breakup date is 10 December).

Antarctic lower stratospheric temperatures were near average in July–September 2022. In October–December 2022, lower stratospheric temperatures were consistently below average (orange line in Fig. 6.15a). The volume of polar stratospheric clouds (PSCs) in 2022 stayed below or near the long-term average during July–October (Fig. 6.15b) and fell to zero as lower stratospheric temperatures rose above the threshold for PSC formation in late September (Figs. 6.15a,b). Heterogeneous chemical reactions occur on polar clouds particle surfaces, releasing chlorine into active forms (e.g., chlorine monoxide, ClO) that deplete ozone at about 1%–2% per day as sunlight returns to the Antarctic in August–September. Aura Microwave Limb Sounder (MLS) observations show that vortex-averaged ClO in 2022 was near or below average until

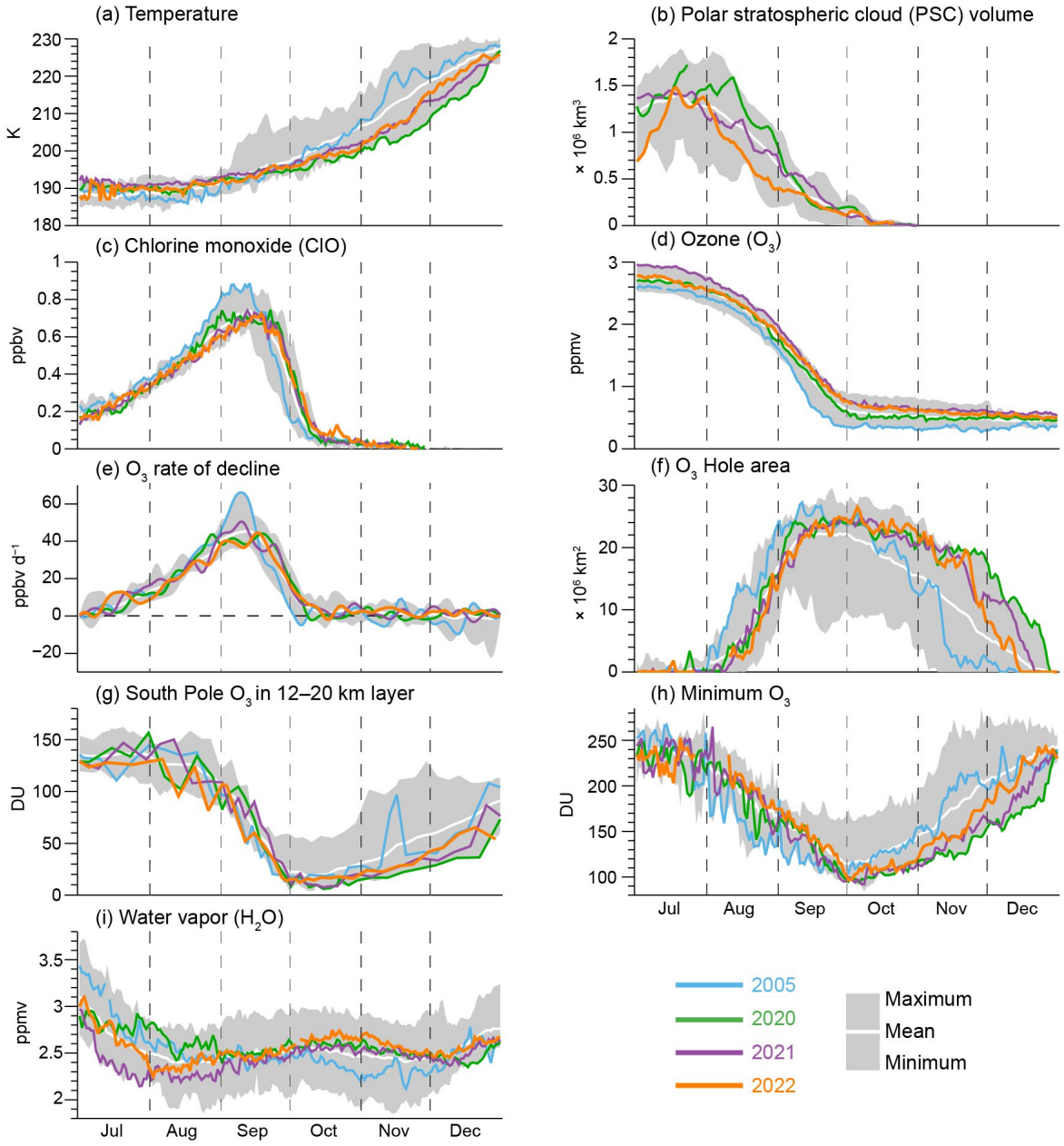

Fig. 6.15. Antarctic values of (a) vortex-averaged MERRA-2 temperature on the 440-K potential temperature surface (~19 km or 60 hPa), (b) CALIPSO polar stratospheric cloud (PSC) volume (updated from Pitts et al. 2018), (c),(d),(e),(i) vortex-averaged chlorine monoxide (ClO), ozone (O_3), O_3 rate of decline (calculated as time derivatives of vortex-averaged ozone), and water vapor (H_2O) on the 440-K potential temperature surface from Aura MLS (updated from Manney et al. 2011), (f) OMI/OMPS Antarctic ozone hole area (area with ozone total column less than 220, DU), (g) lower stratospheric ozone columns (12 km–20 km) based on sonde measurements at South Pole, and (h) minimum total ozone columns over 60°S–90°S from OMI/OMPS. Gray shading shows the range of daily Antarctic values for 2005 (for all but (h), which starts in 2006) through 2021. The white curve indicates the 2005–21 long-term mean. DU is a unit of measurement of the amount of a trace gas in a vertical column. One DU represents the number of trace gas molecules in the 0.01-mm-thick layer at standard atmospheric surface conditions.

mid-September and above average in late September through October (Fig. 6.15c), similar to 2020 and 2021. The seasonal ClO peak was delayed by about a week in 2022. Vortex-averaged ozone on the 440-K isentropic surface (~60 hPa) was above or near average in July–December 2022 (Fig. 6.15d). The seasonal ozone reduction in 2022, estimated by the ozone changes between the first week of July and the first week of October, was about 2.05 ppmv, which is smaller than those in 2020 (2.18 ppmv) and 2021 (2.22 ppmv). The ozone rate of decline (Fig. 6.15e), calculated as time derivatives of vortex-averaged ozone (Fig. 6.15d), is mostly driven by reactive chlorine and bromine from ozone-depleting substances (ODS), with a smaller contribution from transport. The ozone depletion rate is highly correlated with available chlorine (Fig. 6.15c) and typically increases in July–August, reaching its peak between 1 and 20 September with a maximum around 10 September (Strahan et al. 2019). The maximum values of the depletion rate and ClO in the last 18 years were observed in 2005 when the levels of ODS were substantially larger than today. The 2022 ozone rate of decline was close to average.

The Antarctic ozone hole area, defined by the region with total ozone columns below 220 DU, reached its peak of 26.45×10^6 km^2 on 5 October (Fig. 6.15f). Weaker-than-average planetary wave activity in September through early November 2022 prolonged the ozone hole through the October–December period (NASA 2023a). Starting in mid-November, the ozone hole rapidly eroded, disappearing on 16 December. Overall, the ozone hole area in August through early September 2022 was below or near average, consistent with recovery trends of the onset of the ozone hole (Stone et al. 2021) due to ODS decreases.

The lower stratospheric ozone column between 12 km and 20 km derived from sonde measurements at South Pole (SP) station was near or below average in July–September 2022 (Fig. 6.15g), reaching a minimum of 12.4 DU on 5 October. The 2022 minimum total ozone column over the Antarctic (60°S–90°S), measured on 1 and 2 October at 97 DU, was close to the long-term average (Fig. 6.15h). Similar to the situation in 2020 and 2021, both the 12 km–20 km SP column and the minimum Antarctic polar ozone remained below average in October–December 2022 because of the weaker planetary wave activity and below-average lower stratospheric temperatures (Figs. 6.15g,h).

The eruption of the Hunga Tonga-Hunga Ha'apai underwater volcano in January 2022 injected aerosols and a record amount of water vapor directly into the stratosphere. The volcanic material reached altitudes as high as ~55 km–58 km (Carr et al. 2022), and the stratospheric optical depth was the highest since the 1991 Mt. Pinatubo eruption (Taha et al. 2022). While it injected a relatively small amount of sulfur dioxide (~0.4 Tg), Hunga Tonga injected an unprecedented amount of water vapor (146±5 Tg or ~10% of the stratospheric total) into the stratosphere (Millan et al. 2022; Schoeberl et al. 2022). That excess water vapor induced changes in stratospheric temperatures and circulation (Coy et al. 2022). However, MLS observations inside the Antarctic vortex showed near-average water vapor (Fig. 6.15i), indicating that the volcanic plume did not directly affect the 2022 ozone hole's chemical composition.

Antarctic stratospheric ODS levels are slowly declining as a result of the Montreal Protocol (NASA 2023b). Abundances of reactive halogens in the Antarctic stratosphere from the ODSs are estimated using effective equivalent stratospheric chlorine (EESC; Newman et al. 2007). EESC levels in 2022 were 14% lower than the maximum levels observed in the early 2000s. While the reduction in ozone hole severity due to declining ODS concentrations is observable on decadal timescales (Fig. 6.16a), year-to-year ozone hole variations are modulated by Antarctic lower stratospheric temperatures. Temperature effects are estimated by a quadratic fit of EESC with a 5.2-year mean age of air to the observed ozone hole areas (gray line in Fig. 6.16a). Figure 6.16b shows the relationship between September lower stratospheric temperatures and area deviations from the fitted curve. Ozone holes are more severe in colder years (Newman et al. 2004). Below-average September 2022 50-hPa temperatures (green triangle in Fig. 6.16b) increased the area of the ozone hole by 2–3 × 10^6 km^2 with respect to the EESC-fit projection (gray line in Fig. 6.16a). The November hole area also depends on lower stratospheric temperatures (Fig. 6.16d). The 2022 late-spring ozone hole was much larger than average (Fig. 6.15f) because of the late seasonal transition from winter to summer circulation and the associated low temperatures in late spring (Fig. 6.15a), similar to 2020/21.

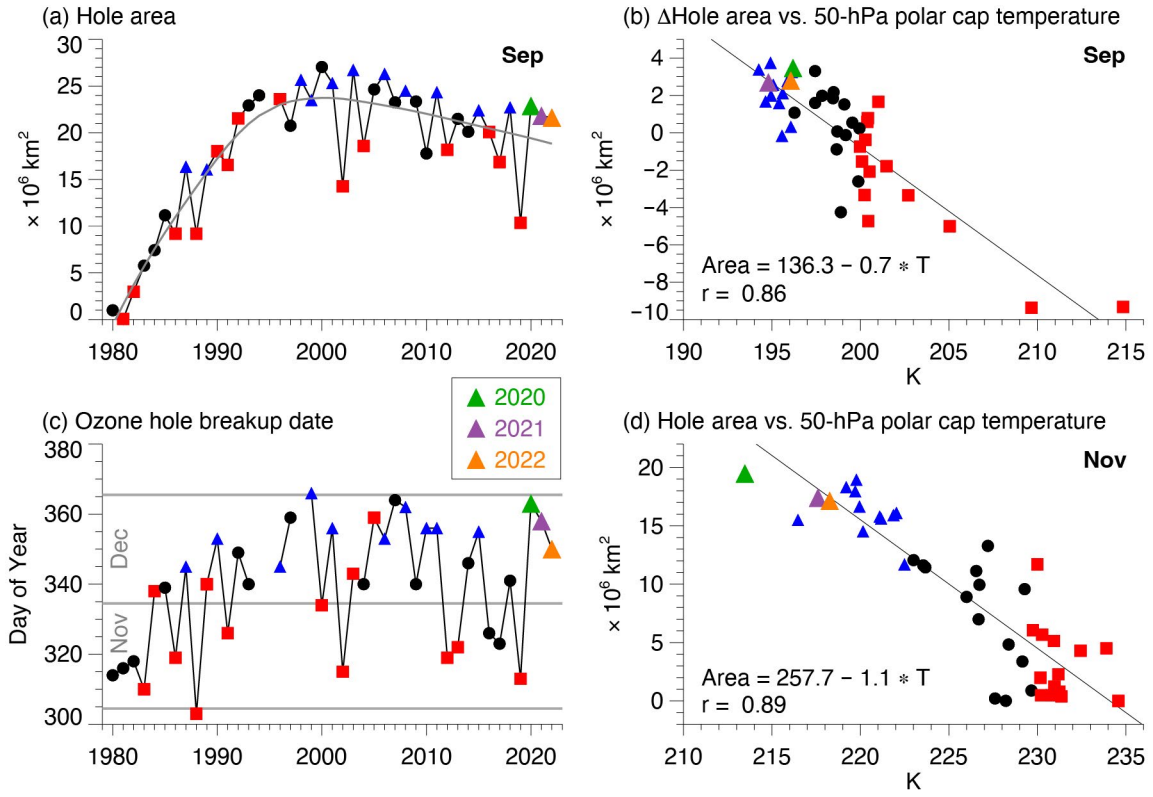

Fig. 6.16. (a) Sep average Antarctic ozone hole area (× 10^6 km^2). (b) Sep anomalies of the ozone hole area (× 10^6 km^2; see text) versus MERRA-2 Sep 50-hPa temperatures (K) averaged over the polar cap (60°S–90°S). (c) Ozone hole disappearance dates (day of yr). (d) Nov ozone hole areas (× 10^6 km^2) versus MERRA-2 Nov 50-hPa temperatures (K). In (a), the gray curve shows a quadratic fit of effective equivalent stratospheric chlorine (EESC) with a 5.2 year mean age of air (Newman et al. 2007) to the Sep hole areas. Years with temperatures in the lowest (highest) third are shown as blue triangles (red squares), and the three years 2020, 2021, and 2022 are highlighted in green, purple, and orange, respectively. Ozone data for 1979–92 are from Total Ozone Mapping Spectrometer (TOMS) Nimbus-7; 1993–94 are from TOMS Meteor-3; 1996–2004 are from EPTOMS, 2005–15 are from Aura Ozone Monitoring Instrument (OMI); and 2015–22 are from Suomi National Polar-orbiting Partnership (SNPP) Ozone Mapping and Profiler Suite (OMPS). There were no satellite total ozone observations for 1995.

The last three austral springs were characterized by very late ozone hole breakups (Fig. 6.16c). These late breakups were caused by anomalously weak planetary wave activity during spring. Planetary waves propagating upward from the troposphere decelerate the polar vortex and force downward motion, warming the vortex. Weak wave activity in 2020, 2021, and 2022 allowed the Antarctic vortex to persist into late spring, keeping stratospheric temperatures below average (Figs. 6.15a,f,g,h). The delay in the vortex breakup in 2022 in turn delayed the ozone hole breakup (Fig. 6.16c). The ozone hole breakup dates are strongly correlated with the vortex breakup dates from 1990 to the present, and in the last three years (2020–22) occurred later than average, producing a statistically significant trend of about 5 days decade^{-1} delay in the ozone hole disappearance. The causes for this trend are not known at this time but potentially can be associated with the strong positive Southern Annular Mode observed in the last three years (see section 6b), which is associated with reduced planetary wave activity. The long-lasting stratospheric vortices in the last three years kept ozone columns below average for October–December and prevented meridional mixing of ozone-rich air from midlatitudes into polar latitudes.

In summary, the 2022 Antarctic ozone hole was slightly larger than average. The large areas of the Antarctic ozone hole in the last three years are consistent with our understanding of ozone depletion and are primarily driven by meteorological conditions. The Hunga Tonga-Hunga Ha'apai eruption did not have a direct effect on the chemical composition of the 2022 ozone hole. The delayed onset in ozone hole area in August–September observed in the last three years is consistent with ozone recovery due to the Montreal Protocol.

Acknowledgments

Work at the Jet Propulsion Laboratory, California Institute of Technology, was done under contract with the National Aeronautics and Space Administration (NASA). Support was also provided by the NASA Modeling and Analysis Program. We are indebted to the many NOAA Corps Officers and GML technical personnel who spend the winters at South Pole Station to obtain the ongoing balloon and ground-based data sets. We also acknowledge the logistics support in Antarctica provided by the National Science Foundation Office of Polar Programs.

- K. R. Clem acknowledges support from the Royal Society of New Zealand Marsden Fund grant MFP-VUW2010.
- J. D. Wille acknowledges support from the Agence Nationale de la Recherche project, ANR-20-CE01-0013 (ARCA).
- R. T. Datta would like to acknowledge NSF award OPP 1952199.
- L. Trusel and R. T. Datta would like to acknowledge NASA award S000885-NASA.
- P. Reid and J. Lieser were supported through the Australian Bureau of Meteorology, and R. Massom by the Australian Antarctic Division. The work of P. Reid and R. Massom also contributes to the Australian Government's Australian Antarctic Partnership Program (AAPP). For R. Massom, this work was also supported by the Australian Research Council Special Research Initiative the Australian Centre for Excellence in Antarctic Science (Project Number SR200100008).
- S. T. Gille acknowledges support from NSF's Southern Ocean Carbon and Climate Observations and Modeling (SOCCOM) Project under the NSF award OPP-1936222.
- L. P. Pezzi acknowledges support from PROANTAR's Antarctic Modeling and Observation System (ATMOS) Project under the CNPq/PROANTAR award 443013/2018-7.
- S. Stammerjohn was supported under NSF PLR–1552226; she also thanks the Institute of Arctic and Alpine Research and the National Snow and Ice Data Center, both at the University of Colorado Boulder, for institutional and data support.
- A. Banwell was supported by NSF award #1841607 to the University of Colorado Boulder.
- N. Ochwat and T. Scambos were supported by NASA award 80NSSC22K0386 on Larsen B evolution and NASA award 80NSSC21K0750 for sea ice monitoring.
- L. M. Keller, M. A. Lazzara, D. E. Mikolajczyk, and T. Norton appreciate support from NSF grant number 1924730, 1951720, and 1951603.

Appendix 1: Chapter 6 – Acronyms

ACC	Antarctic Circumpolar Current
AIS	Antarctic Ice Sheet
AR	atmospheric river
ASL	Amundsen Sea Low
ATLAS	Advanced Topographic Laser Altimeter System
AWS	automated weather station
ClO	chlorine monoxide
CRI	coastal resolution improvement
DO	dissolved oxygen
EESC	effective equivalent stratospheric chlorine
ERA5	European Centre for Medium-Range Weather Forecasts Reanalysis version 5
GRACE	Gravity Recovery and Climate Experiment
GRACE-FO	Gravity Recovery and Climate Experiment Follow-on
H_2O	water
IceSat-2	Ice, Cloud and land Elevation Satellite-2
IVT	integrated water vapor transport
IWV	integrated water vapor
MERRA-2	Modern-Era Retrospective Analysis for Research and Applications version 2
MLD	mixed layer depth
MLS	Microwave Limb Sounder
O_3	ozone
ODS	ozone-depleting substances
OHC	ocean heat content
OMI	Ozone Monitoring Instrument
OMPS	Ozone Mapping and Profiler Suite
PSC	polar stratospheric cloud
PSU	surface salinity
Qnet	net heat flux
SAF	subantarctic front
SAM	Southern Annular Mode
SIA	sea-ice area
SIE	sea-ice extent
SMB	surface mass balance
SMMR	Scanning Multi-Channel Microwave Radiometer
SO	Southern Ocean
SP	South Pole
SSM/I	Special Sensor Microwave Imager
SSMIS	Special Sensor Microwave Imager/Sounder
SST	sea-surface temperature
TOMS	Total Ozone Mapping Spectrometer

References

Adusumilli, S., H. A. Fricker, B. Medley, L. Padman, and M. R. Siegfried, 2020: Interannual variations in meltwater input to the Southern Ocean from Antarctic ice shelves. *Nat. Geosci.*, **13**, 616–620, https://doi.org/10.1038/s41561-020-0616-z.

Agosta, C., and Coauthors, 2019: Estimation of the Antarctic surface mass balance using the regional climate model MAR (1979–2015) and identification of dominant processes. *Cryosphere*, **13**, 281–296, https://doi.org/10.5194/tc-13-281-2019.

Armour, K. C., J. Marshall, J. R. Scott, A. Donohoe, and E. R. Newsom, 2016: Southern Ocean warming delayed by circumpolar upwelling and equatorward transport. *Nat. Geosci.*, **9**, 549–554, https://doi.org/10.1038/ngeo2731.

Arthur, J. F., C. R. Stokes, S. S. R. Jamieson, J. Rachel Carr, A. A. Leeson, and V. Verjans, 2022: Large interannual variability in supraglacial lakes around East Antarctica. *Nat. Commun.*, **13**, 1711, https://doi.org/10.1038/s41467-022-29385-3.

Banwell, A. F., D. R. MacAyeal, and O. V. Sergienko, 2013: Breakup of the Larsen B Ice Shelf triggered by chain reaction drainage of supraglacial lakes. *Geophys. Res. Lett.*, **40**, 5872–5876, https://doi.org/10.1002/2013GL057694.

—— , R. T. Datta, R. L. Dell, M. Moussavi, L. Brucker, G. Picard, C. A. Shuman, and L. A. Stevens, 2021: The 32-year record-high surface melt in 2019/2020 on the northern George VI Ice Shelf, Antarctic Peninsula. *Cryosphere*, **15**, 909–925, https://doi.org/10.5194/tc-15-909-2021.

Baumhoer, C. A., A. J. Dietz, C. Kneisel, H. Paeth, and C. Kuenzer, 2021: Environmental drivers of circum-Antarctic glacier and ice shelf front retreat over the last two decades. *Cryosphere*, **15**, 2357–2381, https://doi.org/10.5194/tc-15-2357-2021.

Beadling, R. L., N. M. Freeman, G. A. MacGilchrist, M. Mazloff, J.-R. Shi, A. F. Thompson, and E. Wilson, 2022: Southern Ocean [in "State of the Climate in 2021"]. *Bull. Amer. Meteor. Soc.*, **103** (8), S329–S332, https://doi.org/10.1175/BAMS-D-22-0078.1.

Bell, R. E., A. F. Banwell, L. D. Trusel, and J. Kingslake, 2018: Antarctic surface hydrology and impacts on ice-sheet mass balance. *Nat. Climate Change*, **8**, 1044–1052, https://doi.org/10.1038/s41558-018-0326-3.

Bevan, S., A. Luckman, H. Hendon, and G. Wang, 2020: The 2020 Larsen C Ice Shelf surface melt is a 40-year record high. *Cryosphere*, **14**, 3551–3564, https://doi.org/10.5194/tc-14-3551-2020.

Carr, J. L., Á. Horváth, D. L. Wu, and M. D. Friberg, 2022: Stereo plume height and motion retrievals for the record-setting Hunga Tonga-Hunga Ha'apai eruption of 15 January 2022. *Geophys. Res. Lett.*, **49**, e2022GL098131, https://doi.org/10.1029/2022GL098131.

Cavalieri, D. J., C. L. Parkinson, P. Gloersen, and H. J. Zwally, 1996: Sea ice concentrations from Nimbus-7 SMMR and DMSP SSM/I-SSMIS passive microwave data, version 1. NASA National Snow and Ice Data Center Distributed Active Archive Center, accessed 3 January 2023, https://doi.org/10.5067/8GQ8LZQVL0VL.

Cheng, L., and Coauthors, 2023: Another year of record heat for the oceans. *Adv. Atmos. Sci.*, **40**, 963–974, https://doi.org/10.1007/s00376-023-2385-2.

Clem, K. R., and M. N. Raphael, Eds., 2022: Antarctica and the Southern Ocean [in "State of the Climate in 2021"]. *Bull. Amer. Meteor. Soc.*, **103** (8), S307–S340, https://doi.org/10.1175/BAMS-D-22-0078.1.

—— , S. Barreira, R. L. Fogt, S. Colwell, L. M. Keller, M. A. Lazzara, and T. Norton, 2022: Atmospheric circulation and surface observations [in "State of the Climate in 2021"]. *Bull. Amer. Meteor. Soc.*, **103**, S313–S316, https://doi.org/10.1175/BAMS-D-22-0078.1.

Comiso, J. C., 2017: Bootstrap sea ice concentrations from Nimbus-7 SMMR and DMSP SSM/I-SSMIS, version 3. NASA National Snow and Ice Data Center Distributed Active Archive Center, accessed 2 February 2023, https://doi.org/10.5067/7Q8HCCWS4I0R.

Coy, L., P. A. Newman, K. Wargan, G. Partyka, S. E. Strahan, and S. Pawson, 2022: Stratospheric circulation changes associated with the Hunga Tonga-Hunga Ha'apai eruption. *Geophys. Res. Lett.*, **49**, e2022GL100982, https://doi.org/10.1029/2022GL100982.

de Boyer Montégut, C., G. Madec, A. S. Fischer, A. Lazar, and D. Iudicone, 2004: Mixed layer depth over the global ocean: An examination of profile data and a profile-based climatology. *J. Geophys. Res.*, **109**, C12003, https://doi.org/10.1029/2004JC002378.

Depoorter, M. A., J. L. Bamber, J. A. Griggs, J. T. M. Lenaerts, S. R. M. Ligtenberg, M. R. van den Broeke, and G. Moholdt, 2013: Calving fluxes and basal melt rates of Antarctic ice shelves. *Nature*, **502**, 89–92, https://doi.org/10.1038/nature12567.

Dunmire, D., and Coauthors, 2020: Observations of buried lake drainage on the Antarctic Ice Sheet. *Geophys. Res. Lett.*, **47**, e2020GL087970, https://doi.org/10.1029/2020GL087970.

—— , J. T. M. Lenaerts, R. T. Datta, and T. Gorte, 2022: Antarctic surface climate and surface mass balance in the Community Earth System Model version 2 during the satellite era and into the future (1979–2100). *Cryosphere*, **16**, 4163–4184, https://doi.org/10.5194/tc-16-4163-2022.

Eayrs, C., X. Li, M. N. Raphael, and D. M. Holland, 2021: Rapid decline in Antarctic sea ice in recent years hints at future change. *Nat. Geosci.*, **14**, 460–464, https://doi.org/10.1038/s41561-021-00768-3.

Fogt, R. L., D. H. Bromwich, and K. M. Hines, 2011: Understanding the SAM influence on the South Pacific ENSO teleconnection. *Climate Dyn.*, **36**, 1555–1576, https://doi.org/10.1007/s00382-010-0905-0.

—— , A. M. Sleinkofer, M. N. Raphael, and M. S. Handcock, 2022: A regime shift in seasonal total Antarctic sea ice extent in the twentieth century. *Nat. Climate Change*, **12**, 54–62, https://doi.org/10.1038/s41558-021-01254-9.

Fraser, A. D., and Coauthors, 2023: Antarctic landfast sea ice: A review of its physics, biogeochemistry and ecology. *Rev. Geophys.*, **61**, e2022RG000770, https://doi.org/10.1029/2022RG000770.

Frölicher, T. L., J. L. Sarmiento, D. J. Paynter, J. P. Dunne, J. P. Krasting, and M. Winton, 2015: Dominance of the Southern Ocean in anthropogenic carbon and heat uptake in CMIP5 models. *J. Climate*, **28**, 862–886, https://doi.org/10.1175/JCLI-D-14-00117.1.

Gelaro, R., and Coauthors, 2017: The Modern-Era Retrospective Analysis for Research and Applications, version 2 (MERRA-2). *J. Climate*, **30**, 5419–5454, https://doi.org/10.1175/JCLI-D-16-0758.1.

Gilbert, E., and C. Kittel, 2021: Surface melt and runoff on Antarctic ice shelves at 1.5°C, 2°C, and 4°C of future warming. *Geophys. Res. Lett.*, **48**, e2020GL091733, https://doi.org/10.1029/2020GL091733.

Gille, S. T., 2002: Warming of the Southern Ocean since the 1950s. *Science*, **295**, 1275–1277, https://doi.org/10.1126/science.1065863.

Glasser, N. F., T. A. Scambos, J. Bohlander, M. Truffer, E. Pettit, and B. J. Davies, 2011: From ice-shelf tributary to tidewater glacier: Continued rapid recession, acceleration and thinning of Röhss Glacier following the 1995 collapse of the Prince Gustav Ice Shelf, Antarctic Peninsula. *J. Glaciol.*, **57**, 397–406, https://doi.org/10.3189/002214311796905578.

Gloersen, P., 2006: Nimbus-7 SMMR polar gridded radiances and sea ice concentrations, version 1. Subset: 37 & 19 GHz, h-polarization, 25 km grid, October 1979–April 1987. NASA National Snow and Ice Data Center Distributed Active Archive Center, accessed 5 May 2020, https://doi.org/10.5067/QOZIVYV3V9JP.

Gomez-Fell, R., W. Rack, H. Purdie, and O. Marsh, 2022: Parker Ice Tongue collapse, Antarctica, triggered by loss of stabilizing land-fast sea ice. *Geophys. Res. Lett.*, **49**, e2021GL096156, https://doi.org/10.1029/2021GL096156.

Gossart, A., S. Helsen, J. T. M. Lenaerts, S. V. Broucke, N. P. M. van Lipzig, and N. Souverijns, 2019: An evaluation of surface climatology in state-of-the-art reanalyses over the Antarctic ice sheet. *J. Climate*, **32**, 6899–6915, https://doi.org/10.1175/JCLI-D-19-0030.1.

Gudmundsson, G. H., F. S. Paolo, S. Adusumilli, and H. A. Fricker, 2019: Instantaneous Antarctic ice sheet mass loss driven by thinning ice shelves. *Geophys. Res. Lett.*, **46**, 13 903–13 909, https://doi.org/10.1029/2019GL085027.

Hersbach, H., and Coauthors, 2020: The ERA5 global reanalysis. *Quart. J. Roy. Meteor. Soc.*, **146**, 1999–2049, https://doi.org/10.1002/qj.3803.

Josey, S. A., J. P. Grist, J. V. Mecking, B. I. Moat, and E. Schulz, 2023: A clearer view of Southern Ocean air-sea interaction using surface heat flux asymmetry. *Philos. Trans. Roy. Soc.*, **A381**, 20220067, https://doi.org/10.1098/rsta.2022.0067.

Kittel, C., and Coauthors, 2021: Diverging future surface mass balance between the Antarctic ice shelves and grounded ice sheet. *Cryosphere*, **15**, 1215–1236, https://doi.org/10.5194/tc-15-1215-2021.

Kramarova, N. A., and Coauthors, 2022: 2021 Antarctic ozone hole [in "State of the Climate in 2021"]. *Bull. Amer. Meteor. Soc.*, **103** (8), S332–S335, https://doi.org/10.1175/BAMS-D-22-0078.1.

Lenaerts, J. T. M., and M. R. van den Broeke, 2012: Modeling drifting snow in Antarctica with a regional climate model: 2. Results. *J. Geophys. Res.*, **117**, D05109, https://doi.org/10.1029/2010JD015419.

—— , B. Medley, M. R. Broeke, and B. Wouters, 2019: Observing and modeling ice sheet surface mass balance. *Rev. Geophys.*, **57**, 376–420, https://doi.org/10.1029/2018RG000622.

Ligtenberg, S. R. M., M. M. Helsen, and M. R. van den Broeke, 2011: An improved semi-empirical model for the densification of Antarctic firn. *Cryosphere*, **5**, 809–819, https://doi.org/10.5194/tc-5-809-2011.

Liu, J., and J. A. Curry, 2010: Accelerated warming of the Southern Ocean and its impacts on the hydrological cycle and sea ice. *Proc. Natl. Acad. Sci. USA*, **107**, 14 987–14 992, https://doi.org/10.1073/pnas.1003336107.

—— , Z. Zhu, and C. Dake, 2023: Lowest Antarctic sea ice record broken for the second year in a row. *Ocean Land Atmos. Res.*, **2**, 0007, https://doi.org/10.34133/olar.0007.

MacFerrin, M., T. Mote, H. Wang, L. Liu, L. Montgomery, and T. Scambos, 2021: Ice sheet seasonal melt extent and duration [in "State of the Climate in 2020"]. *Bull. Amer. Meteor. Soc.*, **102** (8), S331–S334, https://doi.org/10.1175/BAMS-D-21-0081.1.

—— , —— , A. Banwell, and T. Scambos, 2022: Ice sheet seasonal melt extent and duration [in "State of the Climate in 2021"]. *Bull. Amer. Meteor. Soc.*, **103** (8), S321–S323, https://doi.org/10.1175/BAMS-D-22-0078.1.

Maclennan, M. L., and J. T. M. Lenaerts, 2021: Large-scale atmospheric drivers of snowfall over Thwaites Glacier, Antarctica. *Geophys. Res. Lett.*, **48**, e2021GL093644, https://doi.org/10.1029/2021GL093644.

Manney, G. L., and Coauthors, 2011: Unprecedented Arctic ozone loss in 2011. *Nature*, **478**, 469–475, https://doi.org/10.1038/nature10556.

Marshall, G. J., 2003: Trends in the Southern Annular Mode from observations and reanalyses. *J. Climate*, **16**, 4134–4143, https://doi.org/10.1175/1520-0442(2003)0162.0.CO;2.

Maslanik, J., and J. Stroeve, 1999: Near-real-time DMSP SSM/I-SSMIS daily polar gridded sea ice concentrations. National Snow and Ice Data Center, accessed 9 March 2023, https://doi.org/10.5067/U8C09DWVX9LM.

Massom, R. A., A. B. Giles, H. A. Fricker, R. C. Warner, B. Legrésy, G. Hyland, N. Young, and A. D. Fraser, 2010: Examining the interaction between multi-year landfast sea ice and the Mertz Glacier Tongue, East Antarctica: Another factor in ice sheet stability? *J. Geophys. Res.*, **115**, C12027, https://doi.org/10.1029/2009JC006083.

—— , T. A. Scambos, L. G. Bennetts, P. Reid, V. A. Squire, and S. E. Stammerjohn, 2018: Antarctic ice shelf disintegration triggered by sea ice loss and ocean swell. *Nature*, **558**, 383–389, https://doi.org/10.1038/s41586-018-0212-1.

Medley, B., and E. R. Thomas, 2019: Increased snowfall over the Antarctic ice sheet mitigated twentieth-century sea-level rise. *Nat. Climate Change*, **9**, 34–39, https://doi.org/10.1038/s41558-018-0356-x.

Meier, W. N., H. Wilcox, M. A. Hardman, and J. S. Stewart, 2019: DMSP SSM/I-SSMIS daily polar gridded brightness temperatures, version 5. Subset: 37 & 19 GHz, h-polarization, 25 km grid, October 1987–April 2020. NASA National Snow and Ice Data Center Distributed Active Archive Center, accessed 11 February 2021, https://doi.org/10.5067/QU2UYQ6T0B3P.

Millan, L., and Coauthors, 2022: Hunga Tonga-Hunga Ha'apai hydration of the stratosphere. *Geophys. Res. Lett.*, **49**, e2022GL099381, https://doi.org/10.1029/2022GL099381.

Morlighem, M., and Coauthors, 2020: Deep glacial troughs and stabilizing ridges unveiled beneath the margins of the Antarctic ice sheet. *Nat. Geosci.*, **13**, 132–137, https://doi.org/10.1038/s41561-019-0510-8.

Mote, T. L., 2007: Greenland surface melt trends 1973–2007: Evidence of a large increase in 2007. *Geophys. Res. Lett.*, **34**, L22507, https://doi.org/10.1029/2007GL031976.

—— , 2014: MEaSUREs Greenland surface melt daily 25km EASE-Grid 2.0, version 1. NASA National Snow and Ice Data Center Distributed Active Archive Center, accessed 30 August 2021, https://doi.org/10.5067/MEASURES/CRYOSPHERE/nsidc-0533.001.

—— , and M. R. Anderson, 1995: Variations in snowpack melt on the Greenland ice sheet based on passive microwave measurements. *J. Glaciol.*, **41**, 51–60, https://doi.org/10.3189/S0022143000017755.

Mottram, R., and Coauthors, 2021: What is the surface mass balance of Antarctica? An intercomparison of regional climate model estimates. *Cryosphere*, **15**, 3751–3784, https://doi.org/10.5194/tc-15-3751-2021.

NASA, 2023a: OzoneWatch, 45°–75°S 45-day wave 1–3 total eddy heat flux, November monthly mean at 100 hPa. Accessed 10 February 2023, https://ozonewatch.gsfc.nasa.gov/meteorology/figures/merra2/heat_flux/vt1-3w45_75-45s_100_10_merra2.pdf.

——, 2023b: OzoneWatch, what is EESC? Accessed 10 February 2023, https://ozonewatch.gsfc.nasa.gov/facts/eesc_SH.html.

Newman, P. A., S. R. Kawa, and E. R. Nash, 2004: On the size of the Antarctic ozone hole. *Geophys. Res. Lett.*, **31**, L21104, https://doi.org/10.1029/2004GL020596.

——, J. S. Daniel, D. W. Waugh, and E. R. Nash, 2007: A new formulation of equivalent effective stratospheric chlorine (EESC). *Atmos. Chem. Phys.*, **7**, 4537–4552, https://doi.org/10.5194/acp-7-4537-2007.

Norwegian Polar Institute, 2018: Quantarctica v3.0, detailed basemap. www.npolar.no/quantarctica/.

NSIDC, 2022: Antarctic sea ice minimum sets a record. 8 March, http://nsidc.org/arcticseaicenews/2022/03/arctic-sea-ice-approaches-maximum-record-low-minimum-in-the-south/.

Ogle, S. E., V. Tamsitt, S. A. Josey, S. T. Gille, I. Cerovečki, L. D. Talley, and R. A. Weller, 2018: Episodic Southern Ocean heat loss and its mixed layer impacts revealed by the farthest south multiyear surface flux mooring. *Geophys. Res. Lett.*, **45**, 5002–5010, https://doi.org/10.1029/2017GL076909.

Orsi, A. H., T. Whitworth, and W. D. Nowlin, 1995: On the meridional extent and fronts of the Antarctic Circumpolar Current. *Deep-Sea Res. I*, **42**, 641–673, https://doi.org/10.1016/0967-0637(95)00021-W.

Paolo, F. S., H. A. Fricker, and L. Padman, 2015: Volume loss from Antarctic ice shelves is accelerating. *Science*, **348**, 327–331, https://doi.org/10.1126/science.aaa0940.

Pitts, M. C., L. R. Poole, and R. Gonzalez, 2018: Polar stratospheric cloud climatology based on CALIPSO spaceborne lidar measurements from 2006 to 2017. *Atmos. Chem. Phys.*, **18**, 10 881–10 913, https://doi.org/10.5194/acp-18-10881-2018.

Raphael, M. N., 2007: The influence of atmospheric zonal wave three on Antarctic sea ice variability. *J. Geophys. Res.*, **112**, D12112, https://doi.org/10.1029/2006JD007852.

Reid, P. A., and R. A. Massom, 2015: Successive Antarctic sea ice extent records during 2012, 2013 and 2014 [in "State of the Climate in 2014"]. *Bull. Amer. Meteor. Soc.*, **96** (7), S163–S164, https://doi.org/10.1175/2015BAMSStateoftheClimate.1.

——, and R. A. Massom, 2022: Change and variability in Antarctic coastal exposure, 1979–2020. *Nat. Commun.*, **13**, 1164, https://doi.org/10.1038/s41467-022-28676-z.

——, S. Stammerjohn, R. A. Massom, J. Lieser, S. Barreira, and T. Scambos, 2018: Sea ice extent, concentration, and seasonality [in "State of the Climate in 2017"]. *Bull. Amer. Meteor. Soc.*, **99** (8), S183–S185, https://doi.org/10.1175/2018BAMSStateoftheClimate.1.

——, ——, ——, S. Barreira, T. Scambos, and J. L. Lieser, 2022: Sea ice extent, concentration, and seasonality [in "State of the Climate in 2021"]. *Bull. Amer. Meteor. Soc.*, **103** (8), S325–S329, https://doi.org/10.1175/BAMS-D-22-0078.1.

Reynolds, R. W., N. A. Rayner, T. M. Smith, D. C. Stokes, and W. Wang, 2002: An improved in situ and satellite SST analysis for climate. *J. Climate*, **15**, 1609–1625, https://doi.org/10.1175/1520-0442(2002)0152.0.CO;2.

Rignot, E., S. Jacobs, J. Mouginot, and B. Scheuchl, 2013: Ice-shelf melting around Antarctica. *Science*, **341**, 266–270, https://doi.org/10.1126/science.1235798.

Roemmich, D., and J. Gilson, 2009: The 2004–2008 mean and annual cycle of temperature, salinity, and steric height in the global ocean from the Argo Program. *Prog. Oceanogr.*, **82**, 81–100, https://doi.org/10.1016/j.pocean.2009.03.004.

Sallée, J.-B., 2018: Southern Ocean warming. *Oceanography*, **31**, 52–62, https://doi.org/10.5670/oceanog.2018.215.

Scambos, T. A., J. A. Bohlander, C. A. Shuman, and P. Skvarca, 2004: Glacier acceleration and thinning after ice shelf collapse in the Larsen B embayment, Antarctica. *Geophys. Res. Lett.*, **31**, L18402, https://doi.org/10.1029/2004GL020670.

——, E. Berthier, T. Haran, C. A. Shuman, A. J. Cook, S. R. M. Ligtenberg, and J. Bohlander, 2014: Detailed ice loss pattern in the northern Antarctic Peninsula: Widespread decline driven by ice front retreats. *Cryosphere*, **8**, 2135–2145, https://doi.org/10.5194/tc-8-2135-2014.

Schoeberl, M., Y. Wang, R. Ueyama, G. Taha, E. Jensen, and W. Yu, 2022: Analysis and impact of the Hunga Tonga-Hunga Ha'apai stratospheric water vapor plume. *Geophys. Res. Lett.*, **49**, e2022GL100248, https://doi.org/10.1029/2022GL100248.

Seroussi, H., and Coauthors, 2020: ISMIP6 Antarctica: A multi-model ensemble of the Antarctic ice sheet evolution over the 21st century. *Cryosphere*, **14**, 3033–3070, https://doi.org/10.5194/tc-14-3033-2020.

Shepherd, A., and Coauthors, 2012: A reconciled estimate of ice-sheet mass balance. *Science*, **338**, 1183–1189, https://doi.org/10.1126/science.1228102.

Shepherd, J. G., P. G. Brewer, A. Oschlies, and A. J. Watson, 2017: Ocean ventilation and deoxygenation in a warming world: Introduction and overview. *Philos. Trans. Roy. Soc.*, **A375**, 20170240, https://doi.org/10.1098/rsta.2017.0240.

Shi, J.-R., S.-P. Xie, and L. D. Talley, 2018: Evolving relative importance of the Southern Ocean and North Atlantic in anthropogenic ocean heat uptake. *J. Climate*, **31**, 7459–7479, https://doi.org/10.1175/JCLI-D-18-0170.1.

——, L. D. Talley, S.-P. Xie, Q. Peng, and W. Liu, 2021: Ocean warming and accelerating Southern Ocean zonal flow. *Nat. Climate Change*, **11**, 1090–1097, https://doi.org/10.1038/s41558-021-01212-5.

Shuman, C. A., E. Berthier, and T. A. Scambos, 2011: 2001–2009 elevation and mass losses in the Larsen A and B embayments, Antarctic Peninsula. *J. Glaciol.*, **57**, 737–754, https://doi.org/10.3189/002214311797409811.

Smith, B., and Coauthors, 2020a: Pervasive ice sheet mass loss reflects competing ocean and atmosphere processes. *Science*, **368**, 1239–1242, https://doi.org/10.1126/science.aaz5845.

——, and Coauthors, 2020b: ATLAS/ICESat-2 L3A land ice height, version 5. NASA National Snow and Ice Data Center Distributed Active Archive Center, accessed 25 January 2022, https://doi.org/10.5067/ATLAS/ATL06.005.

Smith, T. M., R. W. Reynolds, T. C. Peterson, and J. Lawrimore, 2008: Improvements to NOAA's historical merged land–ocean surface temperature analysis (1880–2006). *J. Climate*, **21**, 2283–2296, https://doi.org/10.1175/2007JCLI2100.1.

Song, X., 2020: Explaining the zonal asymmetry in the air-sea net heat flux climatology over the Antarctic Circumpolar Current. *J. Geophys. Res. Oceans*, **125**, e2020JC016215, https://doi.org/10.1029/2020JC016215.

Spreen, G., L. Kaleschke, and G. Heygster, 2008: Sea ice remote sensing using AMSR-E 89-GHz channels. *J. Geophys. Res.*, **113**, C02S03, https://doi.org/10.1029/2005JC003384.

Squire, V. A., J. P. Dugan, P. Wadhams, P. J. Rottier, and A. K. Liu, 1995: Of ocean waves and sea ice. *Annu. Rev. Fluid Mech.*, **27**, 115–168, https://doi.org/10.1146/annurev.fl.27.010195.000555.

Stammerjohn, S. E., D. G. Martinson, R. C. Smith, X. Yuan, and D. Rind, 2008: Trends in Antarctic annual sea ice retreat and advance and their relation to El Niño–Southern Oscillation and Southern Annular Mode variability. *J. Geophys. Res.*, **113**, C03S90, https://doi.org/10.1029/2007JC004269.

Stone, K. A., S. Solomon, D. E. Kinnison, and M. J. Mills, 2021: On recent large Antarctic ozone holes and ozone recovery metrics. *Geophys. Res. Lett.*, **48**, e2021GL095232, https://doi.org/10.1029/2021GL095232.

Strahan, S. E., A. R. Douglass, and M. R. Damon, 2019: Why do Antarctic ozone recovery trends vary? *J. Geophys. Res. Atmos.*, **124**, 8837–8850, https://doi.org/10.1029/2019JD030996.

Swart, N. C., S. T. Gille, J. C. Fyfe, and N. P. Gillett, 2018: Recent Southern Ocean warming and freshening driven by greenhouse gas emissions and ozone depletion. *Nat. Geosci.*, **11**, 836–841, https://doi.org/10.1038/s41561-018-0226-1.

Taha, G., R. Loughman, P. Colarco, T. Zhu, L. Thomason, and G. Jaross, 2022: Tracking the 2022 Hunga Tonga-Hunga Ha'apai aerosol cloud in the upper and middle stratosphere using space-based observations. *Geophys. Res. Lett.*, **49**, e2022GL100091, https://doi.org/10.1029/2022GL100091.

Tamsitt, V., I. Cerovečki, S. A. Josey, S. T. Gille, and E. Schulz, 2020: Mooring observations of air–sea heat fluxes in two subantarctic mode water formation regions. *J. Climate*, **33**, 2757–2777, https://doi.org/10.1175/JCLI-D-19-0653.1.

Teder, N. J., L. G. Bennetts, P. A. Reid, and R. A. Massom, 2022: Sea ice-free corridors for large swell to reach Antarctic ice shelves. *Environ. Res. Lett.*, **17**, 045026, https://doi.org/10.1088/1748-9326/ac5edd.

The IMBIE Team, 2018: Mass balance of the Antarctic Ice Sheet from 1992 to 2017. *Nature*, **558**, 219–222, https://doi.org/10.1038/s41586-018-0179-y.

Tolman, H. L., 2009: User manual and system documentation of WAVEWATCH III version 3.14. MMAB Rep. 276, NOAA/NCEP, 220 pp., https://polar.ncep.noaa.gov/mmab/papers/tn276/MMAB_276.pdf.

Trusel, L. D., K. E. Frey, S. B. Das, K. B. Karnauskas, P. Kuipers Munneke, E. van Meijgaard, and M. R. van den Broeke, 2015: Divergent trajectories of Antarctic surface melt under two twenty-first-century climate scenarios. *Nat. Geosci.*, **8**, 927–932, https://doi.org/10.1038/ngeo2563.

Trusel, L. D., Z. Pan, and M. Moussavi, 2022: Repeated tidally induced hydrofracture of a supraglacial lake at the Amery ice shelf grounding zone. *Geophys. Res. Lett.*, **49**, e2021GL095661, https://doi.org/10.1029/2021GL095661.

Turner, J., and J. Comiso, 2017: Solve Antarctica's sea-ice puzzle. *Nature*, **547**, 275–277, https://doi.org/10.1038/547275a.

——, T. Phillips, G. J. Marshall, J. S. Hosking, J. O. Pope, T. J. Bracegirdle, and P. Deb, 2017: Unprecedented springtime retreat of Antarctic sea ice in 2016: The 2016 Antarctic Sea Ice Retreat. *Geophys. Res. Lett.*, **44**, 6868–6875, https://doi.org/10.1002/2017GL073656.

——, and Coauthors, 2019: The dominant role of extreme precipitation events in Antarctic snowfall variability. *Geophys. Res. Lett.*, **46**, 3502–3511, https://doi.org/10.1029/2018GL081517.

——, and Coauthors, 2022: Record low Antarctic sea ice cover in February 2022. *Geophys. Res. Lett.*, **49**, e2022GL098904, https://doi.org/10.1029/2022GL098904.

van Wessem, J. M., and Coauthors, 2018: Modelling the climate and surface mass balance of polar ice sheets using RACMO2 – Part 2: Antarctica (1979–2016). *Cryosphere*, **12**, 1479–1498, https://doi.org/10.5194/tc-12-1479-2018.

Wang, H., J. G. Fyke, J. T. M. Lenaerts, J. M. Nusbaumer, H. Singh, D. Noone, P. J. Rasch, and R. Zhang, 2020: Influence of sea-ice anomalies on Antarctic precipitation using source attribution in the Community Earth System Model. *Cryosphere*, **14**, 429–444, https://doi.org/10.5194/tc-14-429-2020.

Wang, J., H. Luo, Q. Yang, J. Liu, L. Yu, Q. Shi, and B. Han, 2022: An unprecedented record low Antarctic sea-ice extent during austral summer 2022. *Adv. Atmos. Sci.*, **39**, 1591–1597, https://doi.org/10.1007/s00376-022-2087-1.

Wang, Y., and Coauthors, 2016: A comparison of Antarctic ice sheet surface mass balance from atmospheric climate models and in situ observations. *J. Climate*, **29**, 5317–5337, https://doi.org/10.1175/JCLI-D-15-0642.1.

Wernli, H., and H. C. Davies, 1997: A Lagrangian-based analysis of extratropical cyclones. I: The method and some applications. *Quart. J. Roy. Meteor. Soc.*, **123**, 467–489, https://doi.org/10.1002/qj.49712353811.

Wiese, D. N., D.-N. Yuan, C. Boening, F. W. Landerer, and M. M. Watkins, 2023a: JPL GRACE mascon ocean, ice, and hydrology equivalent water height RL06.1 CRI filtered version 3. Ver. RL06.1Mv03. PO.DAAC, accessed 10 February 2023, https://doi.org/10.5067/TEMSC-3JC63.

——, ——, ——, ——, and ——, 2023b: Tellus Level-4 ocean mass anomaly time series from JPL GRACE/GRACE-FO mascon CRI filtered release 6.1 version 3. Ver. RL06.1Mv03. PO.DAAC, accessed 10 February 2023, https://doi.org/10.5067/TEMSC-AT613.

Wille, J. D., and Coauthors, 2021: Antarctic atmospheric river climatology and precipitation impacts. *J. Geophys. Res. Atmos.*, **126**, e2020JD033788, https://doi.org/10.1029/2020JD033788.

Zhang, L., T. L. Delworth, X. Yang, F. Zeng, F. Lu, Y. Morioka, and M. Bushuk, 2022: The relative role of the subsurface Southern Ocean in driving negative Antarctic sea ice extent anomalies in 2016–2021. *Commun. Earth Environ.*, **3**, 302, https://doi.org/10.1038/s43247-022-00624-1.

Zhao, X., H. H. Shen, and S. Cheng, 2015: Modeling ocean wave propagation under sea ice covers. *Acta Mech. Sin.*, **31** (1), 1–15, https://doi.org/10.1007/s10409-015-0017-5.